8-2014

Structure Analysis of Sn Bilayer Films on Si (111)

Weisong Tu
University of Tennessee - Knoxville, wtu1@vols.utk.edu

To the Graduate Council:

I am submitting herewith a thesis written by Weisong Tu entitled "Structure Analysis of Sn Bilayer Films on Si (111)." I have examined the final electronic copy of this thesis for form and content and recommend that it be accepted in partial fulfillment of the requirements for the degree of Master of Science, with a major in Physics.

Hanno Weitering, Major Professor

We have read this thesis and recommend its acceptance:

Norman Mannella, Marianne Breinig

Accepted for the Council:
Carolyn R. Hodges

Vice Provost and Dean of the Graduate School

(Original signatures are on file with official student records.)

Structure Analysis of Sn Bilayer Films on Si (111)

A Thesis Presented for the

Master of Science

Degree

The University of Tennessee, Knoxville

Weisong Tu

August 2014

To my wife and thanks for all her sacrifice and support for me

Acknowledgements

I cannot express enough thanks to my committee chair and my advisor, Dr. Hanno Weitering, for his continued support and guidance for my experiment and writing. I also want to show my sincere appreciation to my committee members, Dr. Norman Mannella and Dr. Marianne Breinig, for their suggestion and guidance.

My completion of this project could not have been accomplished without the support of Dr. Daniel Mulugeta and Dr. Paul Snijders. Dr. Daniel Mulugeta taught me how to start my experiment step by step when I first came to lab and shared all his results with me. Dr. Paul Snijders gave me a lot of suggestions and guidance on my research direction and writing.

Thanks to my parents as well, Mr. Fuguo Tu and Mrs. Ruiping Song. The countless times you kept encouraging me and all of your support will not be forgotten.

Finally, to my caring, loving, and supportive wife, Xiaotian Li: my deepest gratitude. I will never forgot your encouragement when the times got rough, your sacrifice of giving up your own career to stay with me when I needed you. I want to show my heartfelt thanks to you.

The only source of knowledge is experience. - Albert Einstein

Abstract

Chemical doping is a well-established method for controlling the electronic properties of bulk semiconductors and, *e.g.*, complex oxide materials. In this process, dopant atoms are located at substitutional lattice locations, from where they introduce free charge carriers to the host material. These carriers greatly improve the electrical conductivity of the host material and can even induce an insulator-metal transition at high doping levels. Dopants, however, also introduce scattering centers that are detrimental to conductivity, especially in low-dimensional systems such as nanowires and ultrathin films. These problems can be overcome by using a modulation doping approach in which the dopant atoms are spatially separated from the conducting layers via heterostructure engineering. In a recent study, Mulugeta and coworkers were able to induce a symmetry-breaking metal insulator transition in an atomic bilayer of Sn on Si(111), by substituting Si atoms in the substrate with boron. However, the structure of the Sn layer is still under dispute and it is not clear where precisely the boron atoms are located and whether the Sn bilayer structure is significantly altered by the boron. The resolve this issue, we performed structure studies on both doped and undoped Sn bilayers, using low-energy electron diffraction (LEED). The intensities of the diffracted beams were recorded as a function of beam voltage and the resulting I(V) curves served as input for the structural refinement with a dynamical diffraction structure code. Various structure models were tested by our collaborators at Penn State University. The structure model proposed by Ichikawa (Ichikawa and Cho, 2003) produces the best fit to the I(V) spectra, although further

refinement remains necessary. Comparison of the I(V) spectra of the doped and undoped Sn layers strongly suggests that the boron atoms are indeed located below the Sn layer. Furthermore, it can be stated with great certainty that the doped and undoped Sn layers have identical structures. Hence, the metal-insulator transition observed by Mulugeta *et al.* can indeed be attributed to carrier doping.

Table of contents

List of Tables

List of Figures

Chapter 1

Introduction

Chemical doping, *i.e.*, the intentional introduction of impurity atoms into a high-purity host material, is a key strategy for modulating the electrical properties of semiconductor materials and devices. The choice of the dopant atom depends on the host material and on the desired functionality. Donor impurities donate extra electrons to the system and the corresponding impurity levels are located just below the conduction band minimum of the semiconductor. Likewise, acceptors introduce valence band holes and the corresponding acceptor levels are located just above the valence band maximum. The energy gap between the dopant levels and the conduction (valence band) continuum equals the binding energy E_B of the electron (hole) to the impurity atom and is relatively small compared to the intrinsic band gap of the semiconductor (Schubert, 1993) .

Group III and Group V elements are the most common dopants for the Group IV semiconductors such as silicon and germanium. By doping pure silicon with a Group V elements, like phosphorus or arsenic, one introduces additional conduction electrons so that the Si or Ge becomes an electrically conductive n-type semiconductor. Doping with Group III elements, which are missing the fourth valence electron, creates "broken bonds" (holes) in the silicon lattice that are free to move as shown in Figure 1.1. This is referred to as p-type doping. Usually, a very heavily doped semiconductor

almost behaves like a metal where the resistivity increases with temperature over a wide temperature range. This effect is commonly used in development of silicon devices such as electronic processors and sensistor (Goodman, 1982). At very high doping levels, the impurity levels form a narrow impurity band. The band width increases with doping concentration and at a critical doping concentration, typically of the order of 10^{20} dopants per cm^3, the impurity band may undergo an insulator-metal transition ("Mott transition"). Alternatively, the Fermi level may move into conduction or valence band continuum of the host material, which is referred to as "degenerate doping". In the former case, the insulator-metal transition is related to the increased screening, at high carrier density, of the attractive Coulomb potential between the dopant ion and charge carriers, which can be viewed as a cooperative many-body phenomenon. The latter case, the insulator metal transition is associated with the overlap of the impurity band and the valence (conduction) band continuum. This is reminiscent of a Bloch-Wilson type transition.

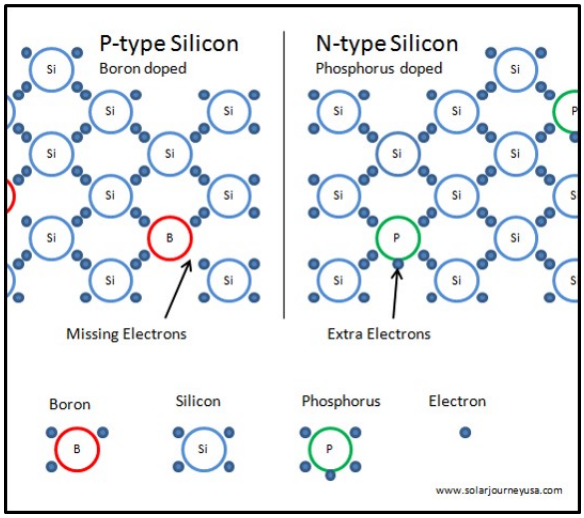

Figure 1.1: The electronic configuration of p-type silicon and n-type silicon (Bogart et al., 2004).

In this thesis, we will expand the doping concept to two-dimensional surface systems. Semiconductor surfaces usually reconstruct and have band structures that are quite different from those in the bulk. The broken bonds at the surface gives rise

to dangling bond surface states in the band gap and in some cases the surface of a semiconductor may even be intrinsically metallic, *i.e.*, without introducing dopants. One of the best known cases is the reconstructed Si(111)7x7 surface. However, metallicy in low-dimensional systems is often very fragile as the system tries to open up a gap at the Fermi level, so as to lower its electronic energy. Because the wavefunction overlap between neighboring dangling bonds is small, the surface state band width is often comparable to the Coulomb repulsion between two electrons in a dangling bond. This strongly suggests that the physics of these systems should be dictated by Mott correlations. Mott insulators defy conventional band theory, which only treats electron correlations at the mean field level. However, when the band width is small, on-site double occupancy is strongly suppressed because of the large on-site Coulomb repulsion. This suppresses carrier hopping and consequently the system is insulating. In particular, the half-filled dangling bonds of the Si(111) and Ge(111) surfaces are ideal model objects for studying the physics of two-dimensional (2D) Mott insulators because the dangling bond states are largely decoupled from the semi-infinite bulk (Tosatti and Anderson, 1974; Flores et al., 1999). Indeed, a recent study of Sn adatoms on the Si (111) surface indicated that this system is a 2D Mott insulator. This phenomenon captured our attention because high temperature superconductivity is established in low dimensional Mott insulators (Tosatti et al., 1995; Lee et al., 2006), and it would be highly desirable to establish high temperature superconductivity on the technologically important Si platform.

Doping of surface layers is a challenge, however. The usual p-type dopants of Si, *i.e.*, the Group-III metal atoms, form well-ordered ($\sqrt{3}$ x $\sqrt{3}$) $R30°$ reconstructions on Si(111), where the metal atoms are located at the T_4 surface locations right above on the second layer Si atoms as shown in Figure 1.2 (Lyo et al., 1989). Because the atoms are trivalent, the dangling bonds of these metal atoms will be empty and, consequently, the system becomes electronically passivated. Importantly, the valence band hole resides in the layer of dopant atoms. Boron, however, is a notable exception. It occupies the S_5 site located right under the T_4 site. The subsurface location is

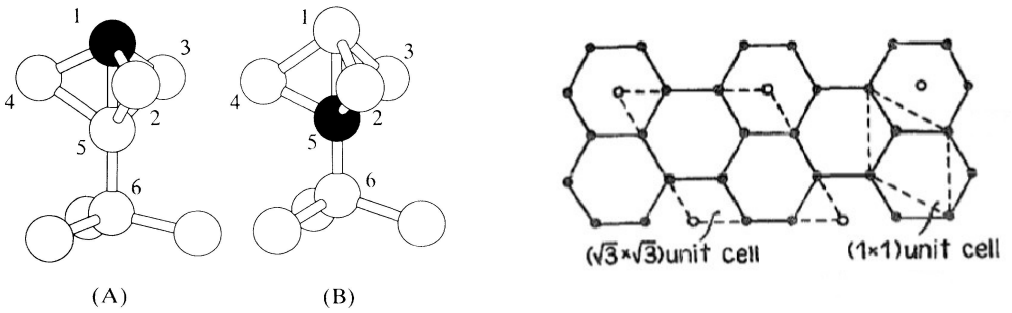

(a) The position of the T_4 adatom, and S_5 adatom adsorption site

(b) Schematic picture of ($\sqrt{3}$ x $\sqrt{3}$) adatom reconstruction with a ball model

Figure 1.2: Schematic picture of T_4 adatom, and S_5 adatom adsorption and ($\sqrt{3}$ x $\sqrt{3}$) adatom reconstruction

favored because the covalent radius of boron is smaller than that of silicon and of the other Group-III elements (Cao et al., 1993). Because boron atoms are trivalent and yet need to form four bonds, electrons are transferred from the Si dangling bonds to the boron atoms beneath the surface. In this case, the hole resides on the Si surface atoms and the dopant atoms are spatially separated from the 2D dangling bond system by at least two bond distances. This situation is much more interesting because it suggests the possibility of hole doping a surface state without disrupting the 2D lattice potential. This doping strategy is analogous to modulation doping in semiconductor heterostructures.

A recent experiment in our group, conducted by Dr. Daniel Mulugeta (D. Mulugeta, Unpublished result), indicated the possibility of forming a ($2\sqrt{3}$ x $2\sqrt{3}$) $R30°$ reconstructed surface layer by depositing 1 ML Sn on Si (111) with and without boron atoms underneath. The introduction of boron beneath the Sn/Si(111) interface did not produce appreciable differences in room temperature scanning tunneling microscopy (STM) images of the Sn layer. This is shown in Figure 1.3a and 1.3b. The surface structures in panels A and B are very similar, which is consistent with the fact that the melting temperatures of the two surfaces are almost identical (Eriksson et al., 2010; Ichikawa and Cho, 2003). However, there are clear differences at low temperature, as shown in panels C and D. The undoped ($2\sqrt{3}$ x $2\sqrt{3}$) $R30°$ Sn layer

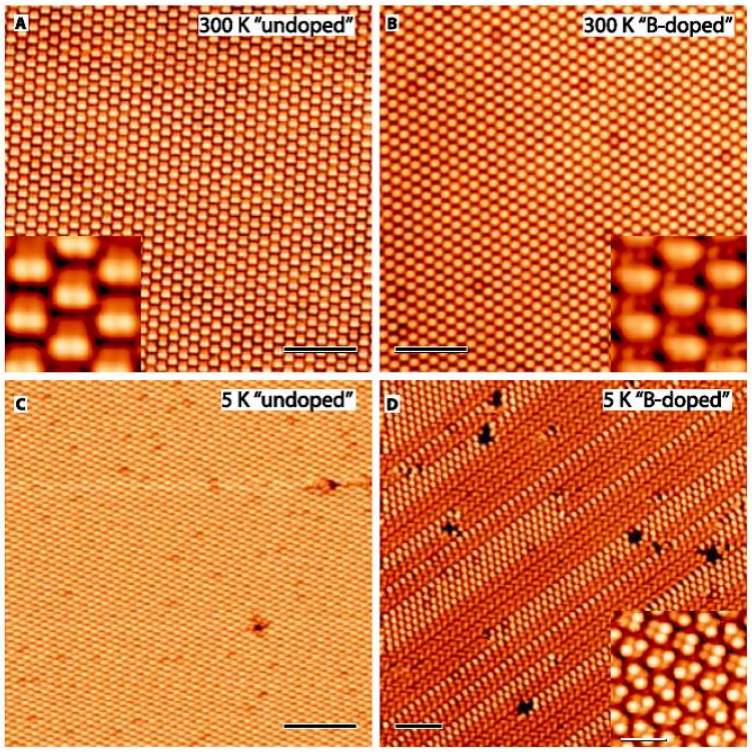

Figure 1.3: STM images of the $(2\sqrt{3}$ x $2\sqrt{3})$ $R30°$ surface with Sn on undoped Si (a,c) and B doped Si (b,d), at room temperature (a,b) and at 5 K (c,d). Scale bars are 8 nm. In (d) the phase with the lower apparent height is the Sn $(4\sqrt{3}$ x $2\sqrt{3})$ $R30°$-B phase. The inset in (d) shows a high-resolution image of the coexisting phases at 5 K.(Mulugeta, Unpublished result)

remains the same at 5K (compare panels A and C). It is insulating up to its melting temperature. On the other hand, the boron doped Sn layer undergoes a reversible metal-insulator transition from an insulating $(4\sqrt{3}$ x $2\sqrt{3})$ $R30°$ structure at low temperature to a metallic $(2\sqrt{3}$ x $2\sqrt{3})$ $R30°$ interface at room temperature. Usually, phase transitions on semiconductor surfaces are of the order-disorder type (Avila et al., 1999; Ortega et al., 2002), but in this case, the phase transition is displacive in nature.

It would seem logical to attribute this displacive insulator-metal phase transition to carrier doping. However, STM images only probe the local density of states and do not provide detailed structural information. Moreover, it turns out that the $(2\sqrt{3}$ x $2\sqrt{3})$ $R30°$ Sn layer is actually a double layer reconstruction. To validate the doping

concept, we need to establish that the Sn layers have identical structure with and without boron atoms present underneath.

The scope of my thesis is to determine whether or not the Sn bilayers are indeed the same. To this end, we studied this system with low-energy electron diffraction (LEED). By recording the intensity of the LEED beams as a function of beam energy, we acquired very large I(V) data sets for detailed structure determination. The latter involves a detailed analysis of the I(V) diffraction data with dynamical diffraction theory. Dynamical diffraction calculations are far more complicated than kinematic diffraction theory used in x-ray diffraction or neutron scattering. These calculations are being performed by our collaborators at Penn State University, who are experts in LEED I(V) structure refinement. While the structure refinement is not yet completed, our results indicate that the atomic structures of the doped and undoped Sn layers are almost identical, and that the boron atoms in the doped system are located at the S_5 lattice locations. Our results strongly support Mulugeta's conjecture that the different electronic properties of the Sn layers should indeed be attributed to a modulation doping.

Chapter 2

Structure Determination with Low-Energy Electron Diffraction (LEED)

One of the most important aspects in surface science is to understand the relationship between the atomic arrangement at the surface and the electronic structure of the surface. In fact, structure-property relationships have always been a centerpiece of condensed matter physics. Logically, the first step in this process is to determine the atomic structure of the surface. Low-Energy Electron Diffraction (LEED) is a commonly used technique to determine the structure of the outermost atomic layers near the surface. In this Chapter, I will introduce concepts related to surface cystallography and discuss both the kinematical and dynamic diffraction theories of LEED.

2.1 Two Dimensional Lattices, Superstructures, and Reciprocal Space

* When we discuss the "surface" of a crystal, we typically imply a three-dimensional entity, because surface reconstructions often extend several atom layers into the bulk. Nonetheless, although the surface region is three-dimensional, the symmetry properties remain two-dimensional (2D) because there is no translational symmetry along the third dimension. Thus, surface crystallography is inherently two-dimensional and one has to consider 2D point groups and 2D Bravais nets, or lattices (VanHove et al., 1986).

Point group operations in 2D include the n = 1, 2, 3, 4 and 6-fold rotations, where the number n describes a rotation by $\frac{2\pi}{n}$. Here, the rotational axes and corresponding mirror planes are perpendicular to the surface (Wood, 1964). The 2D point group operations and 2D translational symmetry define the 2D Bravais lattice. In 2D, there are only five symmetrically distinct Bravais lattices. They are shown in Figure 2.1. Each surface structure can be described by one of these Bravais lattices.

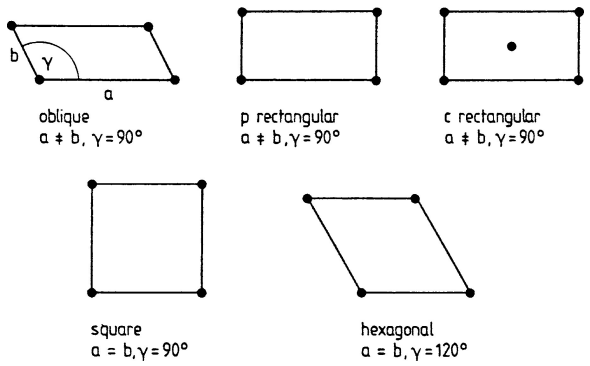

Figure 2.1: Five possible Bravais lattices in 2D space (Luth, 2010)

LEED provides structural information from the outermost layers of the crystal. In our experiments, we are interested in solving the atomic structure of Sn bilayers grown on Si(111). In many cases, deposition of a metal on a semiconductor results in

*H. Lüth, Solid Surfaces, Interfaces and Thin Films, 5th ed., Graduate Texts in Physics, DOI 10.1007/978-3-642-13592-7-3, Springer-Verlag Berlin Heidelberg 2010

a new translational periodicity. In such a situation, the surface unit cell of the film is larger than that of the underlying substrate. Such a superlattice produces additional diffraction beams in LEED. The primitive substrate lattice can be described by a set of 2D translation vectors as:

$$\vec{r}_d = m\vec{a}_1 + n\vec{a}_2 \tag{2.1}$$

Where $d = (m,\ n)$ denotes a pair of integers, and $\vec{a_1}$, $\vec{a_2}$ are the two unit mesh vectors. The surface periodicity of the topmost atomic layer may then be determined in terms of the substrate net by

$$\begin{aligned} \vec{b}_1 &= m_1\vec{a}_1 + n_1\vec{a}_2 \\ \vec{b}_2 &= m_2\vec{a}_1 + n_2\vec{a}_2 \end{aligned} \tag{2.2}$$

We may also represent the relationship with a 2x2 matrix as:

$$\begin{pmatrix} b_1 \\ b_2 \end{pmatrix} = M \begin{pmatrix} a_1 \\ a_2 \end{pmatrix} \tag{2.3}$$

where

$$M = \begin{pmatrix} m_1 & n_1 \\ m_2 & n_2 \end{pmatrix} \tag{2.4}$$

In this case, the determinant of M is det M = m_1n_2-m_2n_1, from which we can obtain the the relation between the surface and substrate lattice. When det M is an integer, the surface lattice is said to be simply related. This is known as a simple superlattice. A superstructure for which det M is a rational number is referred to

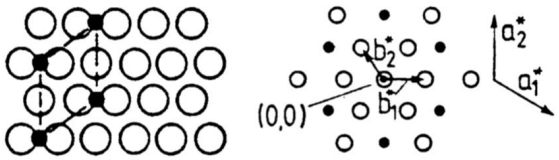

Figure 2.2: Si(111)($\sqrt{3}$ x $\sqrt{3}$)$R30°$ superlattice with the corresponding reciprocal lattice (Luth, 2010)

as a coincidence lattice. In our experiment, the $\sqrt{3}$ x $\sqrt{3}$ superlattice obtained by depositing Sn on Si(111) surface will be similar to the one shown in Figure 2.2.

The reciprocal lattice of a Bravais lattice is the Fourier transform of the real space lattice. In three dimensional cases, if $\vec{a_1}$, $\vec{a_2}$, and $\vec{a_3}$ are the primitive vectors of the crystal lattice, the primitive vectors of the reciprocal lattice $\vec{a_1^*}$, $\vec{a_2^*}$, and $\vec{a_3^*}$ will be:

$$\begin{aligned} \vec{a_1^*} &= 2\pi \frac{\vec{a_2} \times \vec{a_3}}{\vec{a_1} \cdot (\vec{a_2} \times \vec{a_3})} \\ \vec{a_2^*} &= 2\pi \frac{\vec{a_3} \times \vec{a_1}}{\vec{a_2} \cdot (\vec{a_3} \times \vec{a_1})} \\ \vec{a_3^*} &= 2\pi \frac{\vec{a_1} \times \vec{a_2}}{\vec{a_3} \cdot (\vec{a_1} \times \vec{a_2})} \end{aligned} \tag{2.5}$$

In the two dimensional case, the translational vectors of the 2D reciprocal lattice, $\vec{a_1^*}$, $\vec{a_2^*}$ are defined in terms of the real-space bravais lattice vectors $\vec{a_1}$ and $\vec{a_2}$ according to

$$\begin{aligned} \vec{a_1^*} &= 2\pi \frac{\vec{a_2} \times \hat{n}}{\vec{a_1} \times \vec{a_2}} \\ \vec{a_2^*} &= 2\pi \frac{\vec{a_1} \times \hat{n}}{\vec{a_1} \times \vec{a_2}} \end{aligned} \tag{2.6}$$

where $\hat{n}$ is the unit vector normal to the surface. Then

$$\vec{a_i^*} \cdot \vec{a_j} = 2\pi\delta_{ij}, \text{ where } i, j = 1, 2 \tag{2.7}$$

A general translation vector in reciprocal space is given by

$$\vec{G}_{hk} = ha_1^* + ka_2^* \tag{2.8}$$

In this case, the corresponding reciprocal lattice is given by

$$\begin{aligned} \vec{b_1^*} &= h_1^*\vec{a_1^*} + k_1^*\vec{a_2^*} \\ \vec{b_2^*} &= h_2^*\vec{a_1^*} + k_2^*\vec{a_2^*} \end{aligned} \tag{2.9}$$

where

$$\begin{pmatrix} b_1^* \\ b_2^* \end{pmatrix} = M^* \begin{pmatrix} a_1^* \\ a_2^* \end{pmatrix} \tag{2.10}$$

The relationship between matrix M^* and M is

$$M^* = \left(M^{-1}\right)^T \tag{2.11}$$

2.2 Kinematic diffraction theory

LEED is a very important technique to determine the atomic structure of the surface. In a typical LEED experiment, a mono-energetic beam of electrons with energies ranging from 50 eV to 500 eV impinges on the surface at normal incidence. Elastically backscattered electrons form a diffraction pattern and from this pattern, we can determine the symmetry of the surface lattice, simply by visual inspection.

Diffraction spots in LEED patterns originate from Bragg diffracted backscattered electrons. The Bragg condition in 2D is given by two Laue equations. Assuming we have a beam of mono-energetic particles with energy $E = \frac{\bar{h}^2 k^2}{2m}$ and incident wave vector $\vec{k}$, then the scattering vector will be given by $\vec{K} = \vec{k} - \vec{k'}$, where $\vec{k}$ and $\vec{k'}$ are the incident and outgoing wave vector respectively. If the primitive translation vectors of a surface unit cell are $\vec{a}$ and $\vec{b}$, Bragg diffraction occurs when:

$$\begin{aligned} \vec{K} \cdot \vec{a} &= 2\pi h \\ \vec{K} \cdot \vec{b} &= 2\pi k \end{aligned} \tag{2.12}$$

where h and k are integers. If we decompose the scattering vector $\vec{K}$ into parallel and perpendicular components, $\vec{K_\parallel}$ and $\vec{K_\perp}$, we find that

$$\vec{K_\parallel} = \vec{k_\parallel} - \vec{k'_\parallel} = \vec{G_\parallel} \tag{2.13}$$

The vector $\vec{G}_{\parallel}$, as described in equation 2.13, equals to $\vec{G}_{hk}$=h$\vec{a}_1^*$+k$\vec{a}_2^*$, meaning that the parallel component of the scattering vector equals a vector of the 2D surface reciprocal lattice. A common description of scattering in LEED for both 2D and 3D cases uses the Ewald sphere, as shown in Figure 2.3. In the 2D case, this is done by drawing vertical rods through each 2D reciprocal lattice point (h, k). The reciprocal lattice rods signify the lack of translational symmetry normal to the surface in real space. We assume that a wave vector $\vec{k}$ of the primary beam is pointing at the (0,0) reciprocal lattice point. Next, we construct a sphere of radius K so that in the case of elastic scattering, all vectors $\vec{k'}$ point to some location on the sphere. As is seen in Figure 2.3a, the diffraction condition $\vec{K}_{\parallel} = \vec{G}$ is fulfilled when the reciprocal lattice rods intersect the Ewald sphere.

In reality, we should not only consider 2D scattering, as the primary electrons penetrate several atomic layers into the solid. Scattering in the z-direction, which is perpendicular to the surface, will become increasingly three dimensional when electrons penetrate deeper into the bulk. Because these atomic layers have discrete spacings, the reciprocal lattice along the z-direction becomes more discrete. This is illustratred in Figure 2.4. When the Ewald sphere crosses the denser spot-like parts of

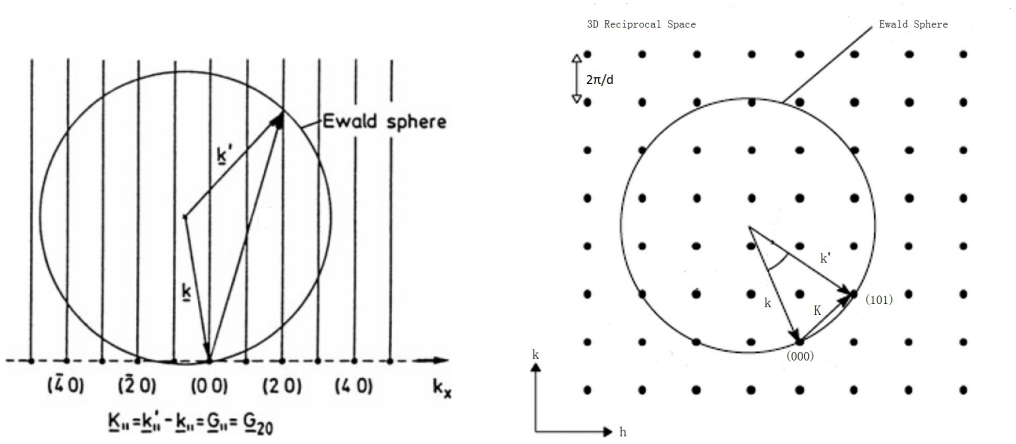

(a) 2 Dimensional **(b)** 3 Dimensional

Figure 2.3: Ewald construction for elastic scattering on a 2D surface surface or in a 3D bulk (Luth, 2010) (VanHove et al., 1986).

the rods, the corresponding Bragg spots will have relatively strong intensity. When the sphere intersects the thin diffuse sectors of the rods, diffraction spots will be weaker (Luth, 2010).

In our experiment, there is another important aspect we need to consider. If we change the primary energy of the incoming electrons, the magnitude of k, which mean the radius of the Ewald sphere, will also change. When $\vec{k}$ is varied, the Ewald sphere passes successively through stronger and weaker regions of the rods, and the intensity of a particular Bragg spot varies periodically. This phenomenon can be verified by measuring the change of intensity of a particular spot as a function of the primary energy energy. This way we record a LEED I(V) curve, where I(V) is the intensity of the diffracted beam at incident beam voltage V. The I(V) curves thus contain structure information.

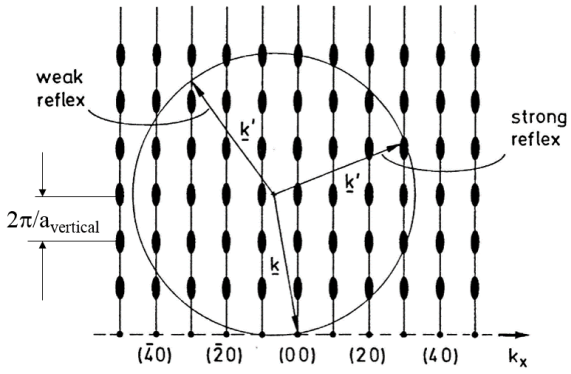

Figure 2.4: Ewald construction for elastic scattering off a quasi-2D surface lattice, as in Figure 2.3, involving several lattice planes. The thicker regions of the rods arise from the third Laue condition, which can no longer be neglected completely (Luth, 2010).

2.3 Dynamical Electron Diffraction

2.3.1 Multiple Scattering and Matching Formalism

†

A typical LEED I(V) curve, obtained by tracking the intensity of the integer order spots of an ultrathin Sn film on Si(111), is shown in Figure 2.5. The most intense peaks are seen at low beam energy. At higher beam energies, electrons penetrate deeper into the bulk and suffer from multiple scattering. To explain the beam intensities in LEED I(V), we need a description of the scattering process beyond the kinematic theory. Multiple-scattering processes take place in the solid, due to the large atomic scattering cross section for low-energy electrons (Luth, 2010). The multiply-scattered electrons also contribute to the LEED spots. To extract atomic structure information from LEED I(V), we need to employ dynamical diffraction theory.

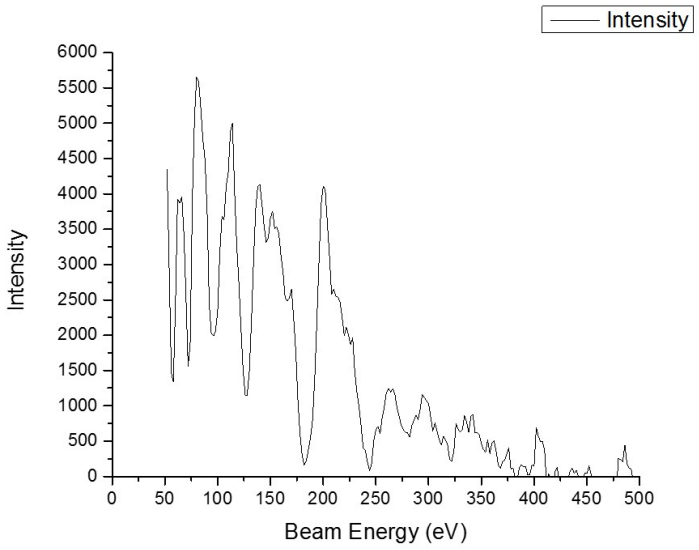

Figure 2.5: LEED I(V) curve from a Sn double layer film on the Si(111):B surface

†M.A.Van Hove, W.H.Weinberg and C.M.Chan, Low-energy electron diffraction experiment, theory and surface structure determination, 6th ed., DOI:10.1002/maco.19870380711, Springer-Verlag Berlin Heidelberg 1986

A straightforward way to solve this problem is by solving the complete Schrödinger equation for a perfect semi-infinite 3D lattice, using Bloch waves satisfying the boundary conditions at the surface. The exact solution for diffraction by a semi-infinite solid then could be obtained by matching these Bloch waves to the wave functions of the incident and the reflected electrons (VanHove et al., 1986).

First, we assume a particle beam is incident upon the surface of a solid. For charged electrons, this surface represents a potential step. Due to the potential difference inside and outside of the solid, electrons will be refracted as shown in Figure 2.6. At the surface plane (z=0) we have the total current I remains unchanged. Since particles do not accumulate at the surface or interface, we have

$$\begin{aligned} I &= I' \\ \vec{j} \cdot \vec{A} &= \vec{j'} \cdot \vec{A} \end{aligned} \tag{2.14}$$

in which $\vec{j}$ and $\vec{j'}$ are the particle current densities on the two sides of the interface and A is the area of the interface that is hit by the beam, as shown in Figure 2.6.

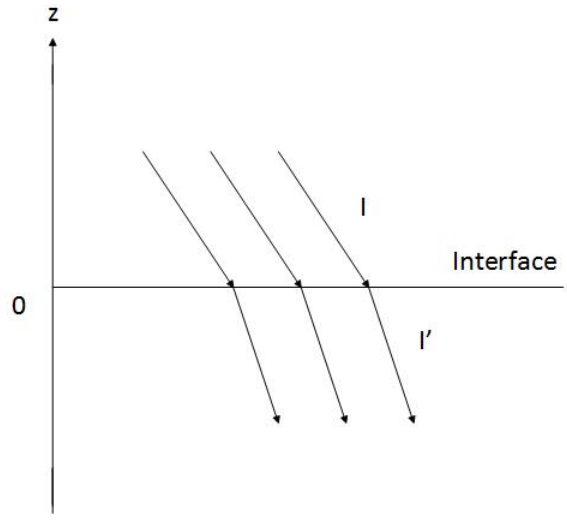

Figure 2.6: A plane-wave electron beam hits an interface at (z = 0) on an area A and is refracted due to a potential step.

From the expansion of of the current density, we obtain

$$\vec{j} = \frac{\hbar}{2im}(\psi^* \nabla\psi - \psi \nabla\psi^*) \tag{2.15}$$

We then apply the matching conditions for the electronic wave functions ψ and ψ'. The wavefunctions and their first derivatives should be continuous at the interface of the crystal, hence:

$$\begin{aligned} \psi|_{z=0} &= \psi'|_{z=0} \\ \frac{\partial}{\partial n}\psi|_{z=0} &= \frac{\partial}{\partial n}\psi'|_{z=0} \end{aligned} \tag{2.16}$$

where $\frac{\partial}{\partial n}$ is the derivative in the direction normal to the surface. With $E = \frac{\hbar^2 k^2}{2m}$ as the incident energy, the primary electrons are described by the wave function

$$\varphi = exp\left[i\vec{k_\parallel} \cdot \vec{r_\parallel} + ik_\perp z\right] \tag{2.17}$$

in which the $\vec{r_\parallel}$ is the parallel component of the electron's position vector and $\vec{k_\parallel}$, $\vec{k_\perp}$ are the components of the incident wave vector $\vec{k}$ parallel and perpendicular to the surface. The energy E is:

$$E = \frac{\hbar^2}{2m}\left(k_\parallel^2 + k_\perp^2\right) \tag{2.18}$$

The full wave function ψ outside the crystal consists of this incoming wave and of the diffracted waves. The surface scattering potential has 2D periodicity. Therefore, upon scattering, $k_\parallel$ is conserved to within a 2D reciprocal lattice vector $G_{parallel} = \vec{G}_{hk} = h\vec{a}_1^* + k\vec{a}_2^*$ and the complete wave-function outside becomes

$$\psi = \varphi + \sum A_{hk} exp\left[i\left(\vec{k_\parallel} + \vec{G_{hk}}\right) \cdot \vec{r_\parallel} - ik_\perp z\right] \tag{2.19}$$

in which the A_{hk} describes the amplitudes of the scattered waves (h, k), and $k_{\parallel}$, $k_{\perp}$ are the wave vectors components parallel and perpendicular to the crystal surface. It follows from energy conservation that:

$$E = \frac{\hbar^2}{2m}\left(\vec{k_{\parallel}} + \vec{G_{hk}}\right)^2 + k_{\perp}^2 \tag{2.20}$$

Within the solid the wavefunctions of the electrons are Bloch waves

$$\psi' = u\left(\vec{r}\right) exp\left(i\vec{k}\cdot\vec{r}\right) = \sum_{\vec{G}} c_{\vec{G}}\left(\vec{k}\right) exp\left[i\left(\vec{k}+\vec{G}\right)\cdot\vec{r}\right] \tag{2.21}$$

in equation 2.21, $\vec{u}_k\left(\vec{r}\right)$ has the periodicity of the 3D lattice, and can therefore be represented as a Fourier series in 3D reciprocal space, and $k_{\parallel}$ $k_{\perp}$ are the wave vectors components parallel and perpendicular to the crystal surface. The coefficients $c_{\vec{G}}\left(\vec{k}\right)$ and the wave vectors $k_{\perp}$ are determined by the periodic potential and the energy. For a certain energy E, which is determined by the acceleration voltage V of the primary beam, the matching conditions can only be fulfilled if there exist electronic states inside the crystal at this energy. The electronic band structure with its allowed and forbidden bands is therefore of considerable importance for the intensity of a particular reflected beam (h, k). If the energy E falls in a forbidden gap of the band structure, the wave functions outside cannot be matched to a Bloch state inside, and a peak in the reflected LEED intensity results.

After solving the complete Schrödinger equation, we can obtain the final solution by considering scattering between different atomic planes, or the inter-layer multiple scattering. To solve this issue, the first thing we need to know is how many layers have to be taken into account. This depends on the penetration depth of primary electrons as illustrated in Figure 2.7. As previously mentioned, the beam energy range of a typical LEED I(V) experiment will be between 50 eV and 500 eV. The wave field between the different atomic layers is composed of sets of forward and backward travelling beams. Forward scattering on the first layer contributes to the

amplitude backscattered at the second layer, and so on. This multiple scattering approach to LEED yeilds essentially the same results as the matching formalism.

2.3.2 The Pendry Reliability Factor and Structure Search

The analysis of experimental data using the dynamic theory of elastic electron scattering is now established as one of the major tools for determinating surface structures. By measuring the distances between the LEED spots and determining the symmetry of the pattern, we can readily determine the lattice spacings and symmetry of the 2D surface lattice. However, if we want to know the precise locations of the surface atoms in the topmost layers, we need to record and analyze the LEED I(V) beams using dynamical diffraction theory. A set of possible atomic coordinates for the atoms in the topmost layers is usually used as input for a dynamic calculation of the I(V) intensities and the results are compared with the experimental data.

Measurement and calculation of the I(V) spectra for a certain structure model is only the first step of a structural analysis. A task of substantial difficulty is still left, namely finding the correct model. One commonly used way to judge whether the model we built fits the experiment LEED I(V) data is to compute the Reliability Factor of the fit. The Reliability factor (so called R-factor) is used to measure the

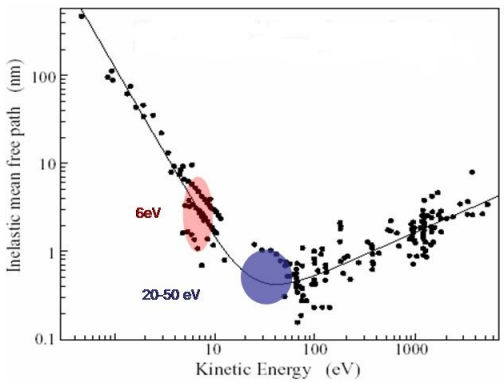

Figure 2.7: Mean free path of electrons in solids as a function of their energy (Seah and Dench, 1979)

agreement between the experimental and theoretical I(V) data (Morris et al., 1992). Due to the complex structure of the spectra, different R-factor definitions have been used. Today, the relative mean square deviations of intensities(R_2) or Pendry R-factor(R_P) is the mostly widely used reliability measure. In both cases the summation is over all intensities $I_g(E_i)$ taken for different beams g and at different energies E_i (Pendry, 1980). So R_2 simply results by

$$R_2 = \frac{\sum_{i,g} \left(cI_{cal} - I_{exp}\right)^2}{\sum_{i,g} I_{exp}^2} \tag{2.22}$$

Where c is the average normalization constant between the experimental and calculated spectra. The Pendry R-factor is more sophisticated and follows the idea that maxima and minima in the spectra are the most important features (Pendry, 1980). Their positions correspond to constructive and destructive interference conditions, which depend both on the electron wavelength and path length difference between different interfering diffraction processes. Therefore, emphasis is on the positions of the maxima and minima rather than on the absolute magnitude of the intensities. So, instead of the intensities, their logarithmic derivative with respect to energy is used

$$L = \frac{\frac{\partial I}{\partial E}}{I} \tag{2.23}$$

Because for small intensities L is very sensitive to experimental errors, the bounded function

$$Y = \frac{L}{\left[1 + \left(LV_{0i}\right)^2\right]} \tag{2.24}$$

is used instead of L. V_{0i} is the so-called inner potential. The Pendry R-factor is then taken as the mean square deviations of the Y functions instead of the intensities, as in the case of R_2

$$R_P = \frac{\sum_{i,g} \left(Y_{cal} - Y_{exp}\right)^2}{\sum_{i,g} \left(Y_{cal}^2 + Y_{exp}^2\right)} \tag{2.25}$$

Ideal agreement corresponds to $R_P = 0$, uncorrelated spectra yield $R_P = 1$ and anti-correlated curves produce $R_P = 2$. The variance of the Pendry R-factor

$$var\,(R_P) = R_{P,min}\left(\frac{8V_{0i}}{\Delta E}\right)^{\frac{1}{2}} \tag{2.26}$$

where ΔE is the energy width of the total data base, allows estimation of the error limits for the model parameters determined (Pendry, 1980).

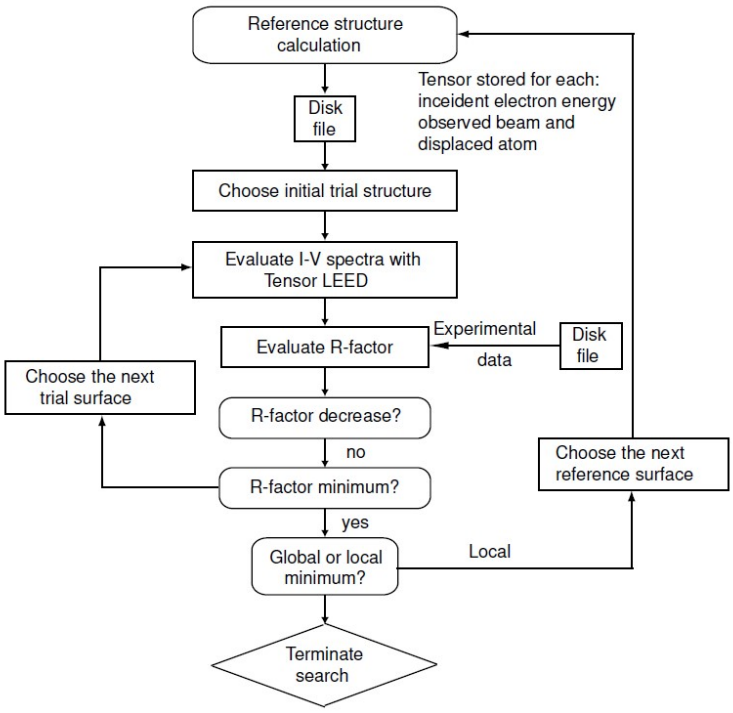

Figure 2.8: The procedure to fit a surface structure model depend on LEED I(V) data

Once a reasonable and promising model is established, the parameters of this model need to be adjusted. There are several ways for this procedure, which are based on a trial-and-error approach, whereby scanning the parameter space is the most basic procedure. When a large number of parameters on a dense grid has to be scanned, the necessary computational efforts grow dramatically and an automated search for the best fit is needed. As shown in Figure 2.8, we can start with a certain

reference structure. The behavior of the R-factor in the surrounding part of the parameter space is explored to find the direction in which the R-factor decreases the most and this procedure is then iterated. After several trails and tests, the Pendry R-factor ideally should reach a global minimum. The corresponding structure model is then the best fit to the LEED I(V) data.

Chapter 3

Experimental Equipment and Procedures

*

In this Chapter, I will introduce the Ultra-High Vacuum (UHV) system and techniques I used in my experiments such as Molecular Beam Epitaxy (MBE), LEED, Scanning Tunneling Microscopy (STM) and X-ray Photoelectron Spectroscopy (XPS).

3.1 The UHV chamber and pumping system

Ultra-High Vacuum (UHV) techniques are critical in surface and interface physics. UHV is essential for preparing atomically clean surfaces and to maintain surface cleanliness for many hours during which the experiments take place. The pressure in a UHV system is in the low 10^{-10} mbar range. A typical UHV chamber consists of a stainless-steel vessel in which we conduct our experiments, including sample preparation, thin film growth, XPS, LEED and STM. Figure 3.1 shows the OMICRON UHV system with a DAR 400 X-ray Source that was used in my experiments.

*H. Lüth, Solid Surfaces, Interfaces and Thin Films, 5th ed., Graduate Texts in Physics, DOI 10.1007/978-3-642-13592-7-3, Springer-Verlag Berlin Heidelberg 2010

To maintain the pressure is the low 10^{-10} mbar range, several types of pumps are needed. Each of these operates in a limited pressure range so we need a combination of different pumps to reach 10^{-10} mbar. As shown in Figure 3.2, the combination of a rotary pump, turbo-molecular pump, and an ion pump spans the pressure gap between UHV and atmospheric pressure. The rotary pump functions on the basis of changing gas volumes produced by the rotation of an eccentric rotor. The operating principle of a turbo-molecular pump is based on the action of a high-speed rotor (15000 to 30000 rpm) which scatter gas molecules from the UHV chamber to the back side of the pump, where they are pumped away by the rotary pump. Ion-getter pumps are very convenient as standby pumps for maintaining UHV conditions for an extended period of time. Gas molecules are ionized and the ions formed are accelerated to a Ti cathode where they are captured or chemisorbed. Due to their high energies they penetrate into the cathode material and sputter Ti atoms away, which then settle on the anode surfaces where they also trap residual gas atoms (Luth, 2010). The titanium pump consists of a titanium filament through which a high current

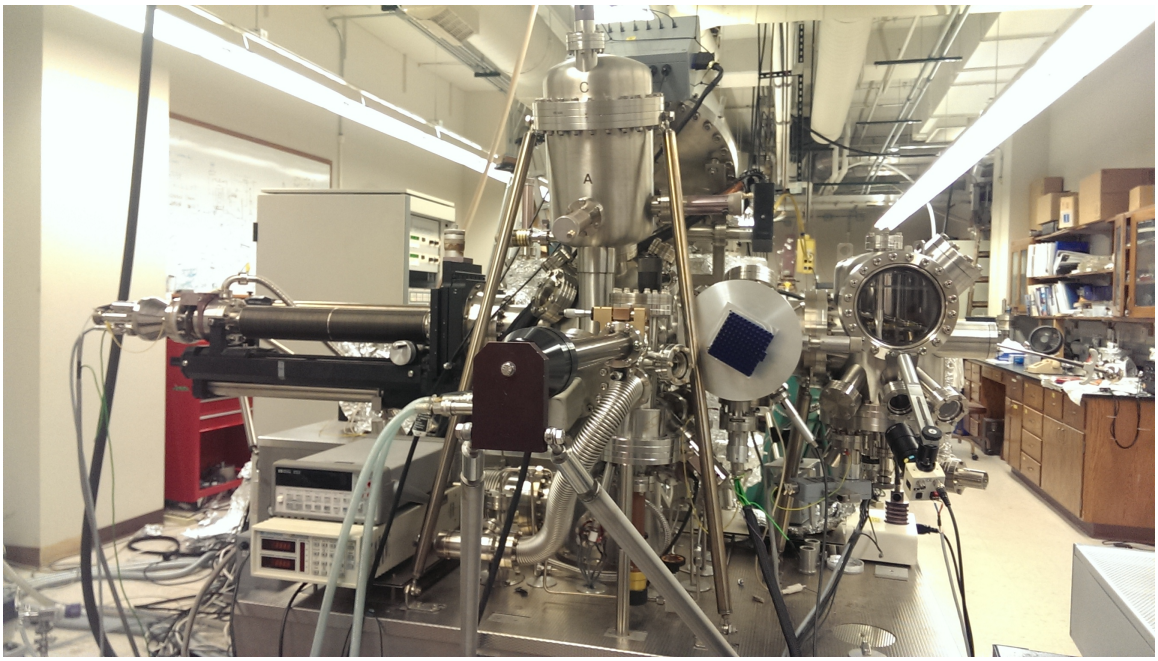

Figure 3.1: Photo of the OMICRON UHV system with integrated DAR 400 X-ray source

(48 Amps on my chamber) is passed periodically (32 hours). This current causes the filament to reach the sublimation temperature of titanium, and the surrounding chamber walls become coated with a thin film of clean titanium. Since pure titanium is very reactive, residual gas molecules in the chamber that collide with the chamber walls are likely to react and to form a stable, solid product. Thus the gas pressure in the chamber is reduced (Redhead et al., 1993).

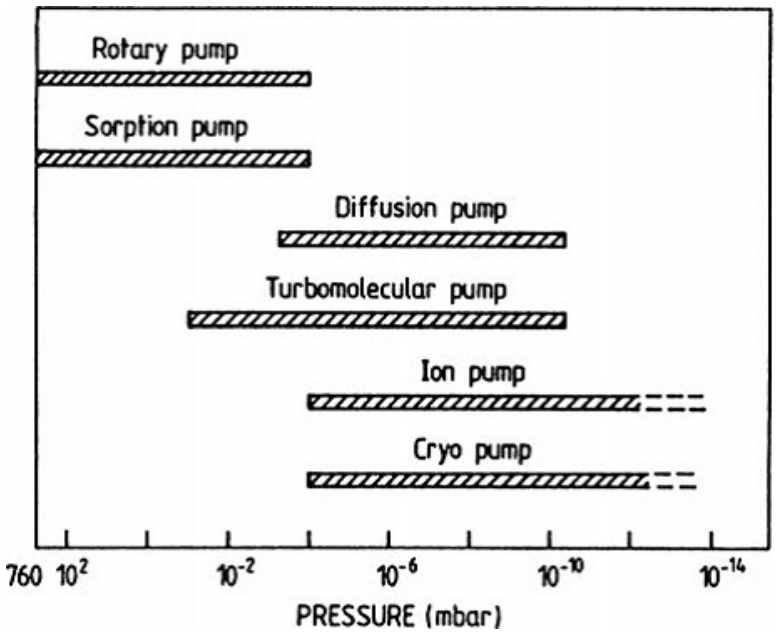

Figure 3.2: Pressure ranges in which different types of pumps can be employed (Luth, 2010)

Initial pump down starts with the rotary pump, which pumps out the air through the turbo pump. Once the pressure is in the 10^{-2} mbar range, it is safe to turn on the turbo pump. It is essential to maintain a pressure of 10^{-2} mbar in between the two pumps. Thus, the rotary pump serves as the backing pump for the turbo pump. Once the chamber pressure is in the 10^{-6} mbar range, we bake the chamber at 160°C. for up to 48 hours. The bake releases gas molecules from the interior walls, which are pumped away by the turbopump. After cooling the chamber to room temperature, we turn on the ion pump and the pressure drops to the UHV range. When reaching UHV operating pressure, we close the valve between the main chamber and turbo

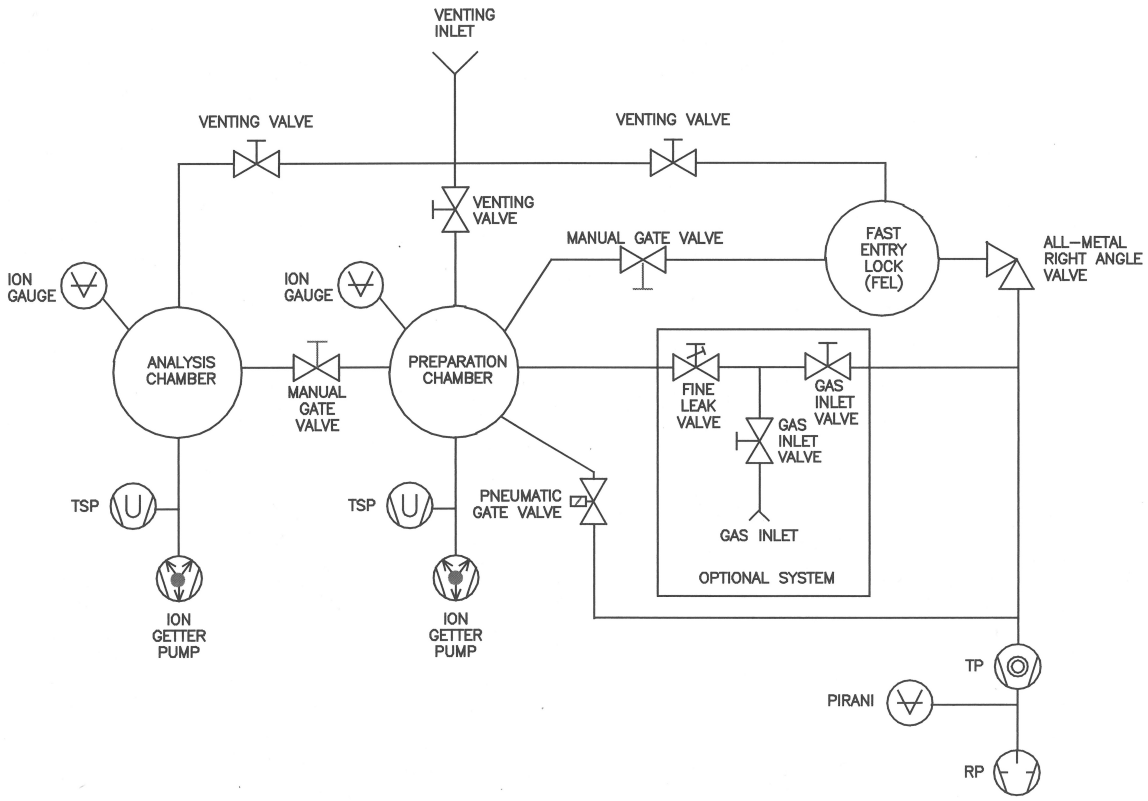

Figure 3.3: Schematic view of the OMICRON ultra-high vacuum (UHV) system

pump, allowing the chamber to be pumped by ion pump and titanium sublimation pump (TSP). The TSP is essential for bringing down the pressure into the 10^{-11} mbar range. Four pressure gauges covering different pressure ranges are also installed on this chamber. A schematic of the pumping system is shown in Figure 3.3.

3.2 Molecular Beam Epitaxy (MBE)

There are many ways to deposit thin films in an UHV environment. One method is to evaporate atoms or molecules from a hot effusion cell onto an atomically clean crystalline substrate. Depending on the substrate surface and evaporation conditions, these sublimated films can be mono-crystalline. Molecular Beam Epitaxy (MBE) is such a method for growing single crystal epitaxial films. Freshly deposited epitaxial

films grown under UHV conditions are very pure and have negligible contamination, so they are ideal materials for surface studies. Hence, MBE is one of the most important techniques for preparing clean thin film surfaces, especially for growing sharp interfaces and heterostructures of elemental semiconductors such as silicon, germanium, or compound semiconductors such as the group III-V semiconductors (Luth, 2010). Researchers are interested in these materials because of their technological relevance. In our work, we are interested in growing novel 2D materials for fundamental studies of their structural and electronic properties.

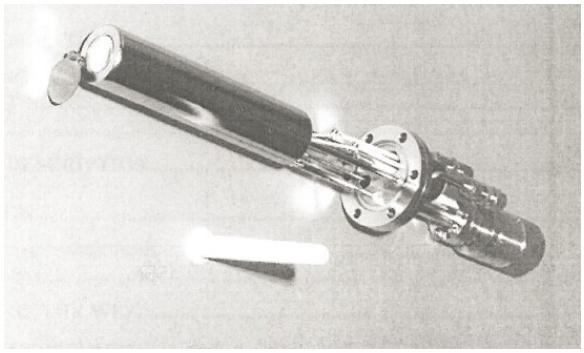

Figure 3.4: Effusion cell with mounting flange, water-cooled shroud, beam shutter, and PBN crucible.

In our experiment, we deposited Sn on a well ordered-boron doped silicon ($\sqrt{3}$ x $\sqrt{3}$) R30° surface. 99.99 percent pure tin is loaded into a ceramic crucible, which

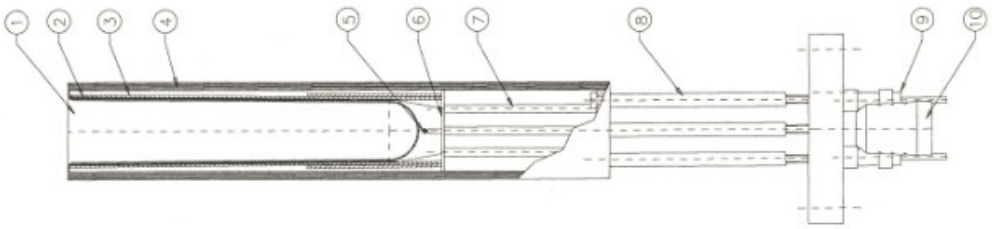

Figure 3.5: Interior of a Knudsen-type effusion cell

we place inside a Knudsen-type effusion cell, as shown in Figure 3.4. A schematic drawing of the K-cell is shown in Figure 3.5. The crucible is inserted at position 1. It is surrounded by a Ta heating filament (2). On the outside of the heating filament, there are several tantalum radiation shields (4) that are mounted on a tantalum base plate (6). The temperature of the crucible is measured with a thermocouple (5). A water cooling shroud is used to minimize radiative heating of the chamber walls, which would otherwise degas tremendously and raise the chamber pressure to unacceptable levels. The K-cell is capped with a diaphragm and shutter that are both made out of molybdenum. Small diaphragm apertures are needed to establish quasi equilibrium inside the K-cell and to control the molecular beam profile. A shutter is needed to interrupt the beam flux without shutting down the K-cell. This is important as it often takes a long time to stabilize the K-cell temperature. In our experiment, the evaporation temperature is around 950°C. The tin will melt at that temperature and evaporate through the aperture.

3.3 Low-Energy Electron Diffraction (LEED)

LEED is used to determine the surface structure. A typical experimental set up for LEED is shown in Figure 3.6. The incident electron beam is produced by an electron gun with a cold thoriated tungsten cathode. It can produce electron beams with beam energies between 20 eV and 500 eV. The backscattered electrons are accelerated to a fluorescent screen, which is kept at a voltage of +5 keV. The screen lights up upon impact and the resulting spot pattern is a direct image of the 2D reciprocal lattice.

The wavelength λ of the incident and elastically scattered electrons can be calculated from the de Broglie relation

$$\lambda = \frac{h}{\sqrt{2mE}} \tag{3.1}$$

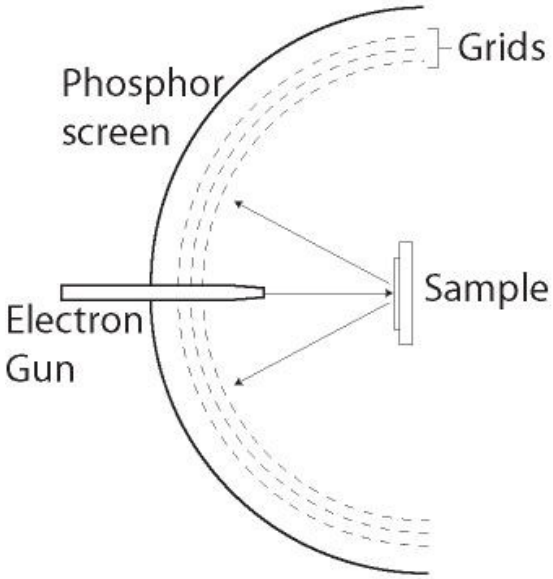

Figure 3.6: Schematic picture of a LEED system

Here, h is Planck's constant, m is the mass of a free electron and E is the beam energy. Hence, we can write

$$\lambda = \sqrt{\frac{150}{E}} \tag{3.2}$$

where λ is given in $\mathring{A}$ngstrom and E is given in eV. The wavelength in LEED is comparable to the interatomic distances in a solid. In addition, the inelastic mean free path inside the solid is only a few atomic layer spacings (Chapter 2), and hence, LEED is very well suited for surface crystallography studies. (Pendry, 1974)

The kinematic diffraction process can be well explained with the Ewald sphere construction, as discussed in Chapter 2. The condition for constructive interference and, consequently, the formation of a spot pattern on the LEED screen is given by $\vec{k'} - \vec{k} = \vec{G}(hkl)$, where $\vec{G}(hkl)$ is a reciprocal lattice vector.

The LEED pattern is recorded by a charge-coupled device (CCD) camera. The sensor of a CCD camera usually contains two regions. One is the photoactive region, which is made of an epitaxial layer of silicon. The other region is the transmission region, which contains a shift register. When the CCD captures the image, the light is projected through a lens onto the photoactive region, which causes each capacitor

to accumulate an electric charge proportional to the light intensity at that location. A one-dimensional array, used in line-scan cameras, captures a single slice of the image, while a two-dimensional array, used in video and still cameras, captures a two-dimensional picture corresponding to the scene projected onto the focal plane of the sensor (Boyle and Smith, 1970). Once the array has been exposed to the image, a control circuit causes each capacitor to transfer its contents to the transmission region. The last capacitor in the array dumps its charge into a charge amplifier, which converts the charge into a voltage. This procedure is shown in the Figure 3.7. By repeating this process, the control circuit converts the entire content of the array in the semiconductor to a sequence of voltages. In a digital device, these voltages are then sampled, digitized, and usually stored in memory; in an analog device (such as an analog video camera), they are processed into a continuous analog signal which is then processed and fed to other circuits for transmission, recording, or other processing.

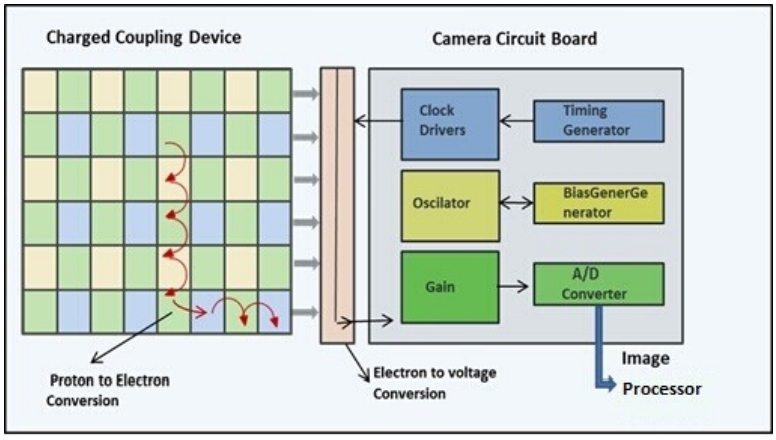

Figure 3.7: Schematic of working procedure of CCD camera

3.4 Scanning Tunneling Microscopy (STM)

STM is a very important technique to scan the atomic scale topography of a solid surface. The theory of STM is based on the concept of quantum tunneling. When a conducting tip approaches a conducting surface to within one nanometer, a bias

(voltage difference) applied between the tip and the surface allows electrons to tunnel through the vacuum barrier separating the two conductors. The resulting tunneling current is a function of the tip position, applied voltage, and the local density of states (DOS) (Chen, 1993). The atomic scale topography of the surface is obtained by recording the tunneling current as a function of the lateral position on the surface. The tunnel current is given by:

$$I_T \propto \frac{U}{d} exp\left(-Kd\sqrt{\bar{\phi}}\right) \tag{3.3}$$

where U is the applied voltage between the two electrodes (tip and sample), $\bar{\phi}$ is the average work function ($\bar{\phi} \gg$ eU), and K is a constant of the vacuum gap, which has a value of about 1.025 x $\mathring{A}^{-1} \cdot (\text{eV})^{-1/2}$. I_T is easily measurable for distances d of the order of several of Angstroms, which can be controlled with a precision of 0.05 to 0.1 $\mathring{A}$ (Luth, 2010). If the tip is moved across the sample in the x-y plane, the variations in surface height and density of states cause lateral variations in the tunneling current. These changes are mapped to create real space images. The change

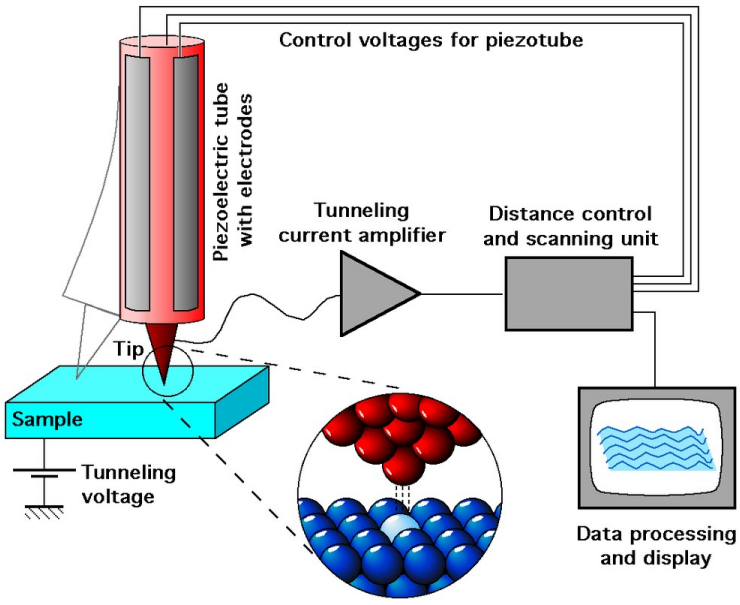

Figure 3.8: Schematic view of an STM (Oura et al., 2003)

in current with respect to lateral position can be measured directly. Alternatively, one can measure the height, z, of the tip while maintaing a constant current during the scan (Oura et al., 2003). A typical STM contains a tiny metal tip, usually made of Tungsten, which is attached to a piezo electric element that can expand or contract into three dimensions. A coarse sample-to-tip control, a vibration isolation system, and computer are included in a typical STM set up (Figure 3.8).

3.5 X-ray Photoelectron Spectroscopy (XPS)

X-ray Photoelectron Spectroscopy (XPS), also known as ESCA (electron spectroscopy for chemical analysis), is a surface-sensitive quantitative spectroscopic technique that measures the chemical composition, chemical valence states, and electronic properties of the surface region of the material. XPS spectra are obtained by irradiating a material with a monochromatized beam of X-rays, while simultaneously measuring the kinetic energy and number of electrons that escape from the topmost layers of the surface, as shown in Figure 3.9. Since we know the X-ray photon energy and the

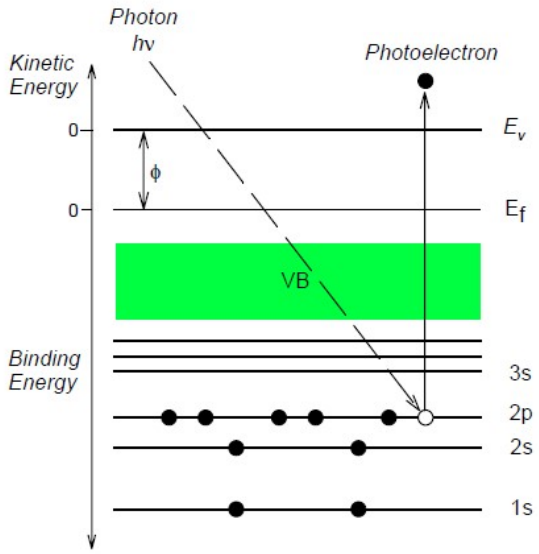

Figure 3.9: Schematic of the analytical method of XPS (Oura et al., 2003)

kinetic energy of the outgoing photoelectron, we can calculate the binding energy of the photoionized levels, using Equation 3.4.

$$E_{binding} = h\nu - (E_{kinetic} + \phi) \tag{3.4}$$

in this equation, $E_{binding}$ is the binding energy (BE) of the electron and $h\nu$ is the energy of the X-ray photons. We use an Al- Kα X-ray source ($h\nu$ =1486.6eV). $E_{kinetic}$ is the kinetic energy of the photoelectron and ϕ is the work function of of the spectrometer.

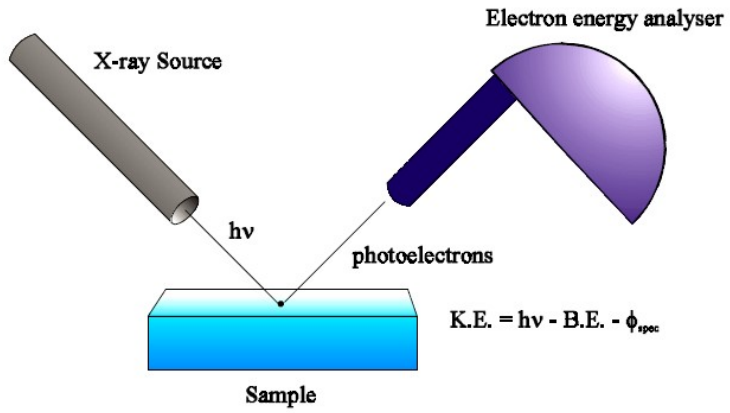

Figure 3.10: Schematic view of an XPS equipment (Oura et al., 2003)

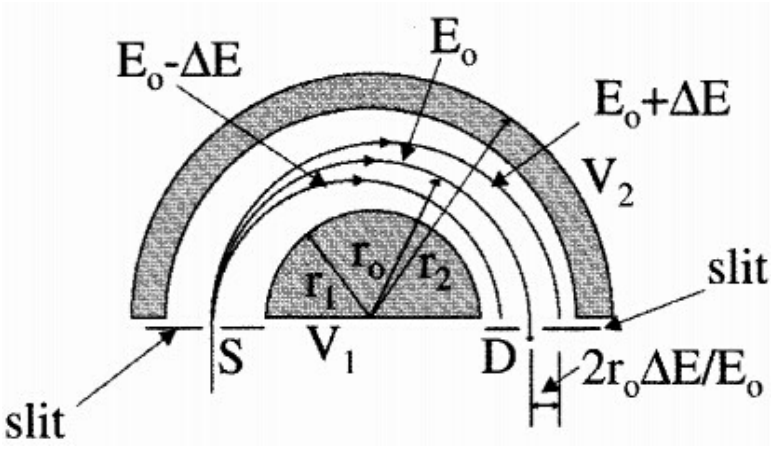

Figure 3.11: Schematic of the interior picture of a XPS analyzer (Oura et al., 2003)

The EA 125 hemispherical kinetic energy analyzer is equipped with a multi-element electrostatic lens with a 30 mm working distance. The lens is used to collect electrons from the sample and focus them onto the entrance of the analyzer. A set of slits at the analyzer entrance controls the transmission characteristics and resolution of the analyzer. The analyzer itself consist of two concentric hemispheres with a 125 mm mean radius. Photoelectrons are dispersed by applying a bias between the hemispheres so that only electrons with a specific kinetic energy (depending on the bias) will exit the analyzer and reach a linear electron multiplier array, which is shown in the Figure 3.11 . The number of channel electron multipliers in the array can be set to 1, 5 or 7 using the exit slits (Figure 3.10).

Chapter 4

Growth and LEED IV Data Acquisition of the Si(111) ($2\sqrt{3}$ x $2\sqrt{3}$) R30°:Sn reconstruction on n-type and p-type silicon

4.1 Growth and characterization of Sn on n-type Si

4.1.1 Introduction

There are many reports in the literature concerning the growth and structure of tin on silicon. Low-energy electron-diffraction (LEED) and scanning tunneling microscopy (STM) show that Sn on Si (111) forms various surface reconstructions, with coverages ranging from one-third monolayer up to one full monolayer (1ML = 7.8 x 10^{14} atoms per cm^2, the density of atoms in the ideal Si(111) surface plane) (Tornevik et al., 1991). A $\frac{1}{3}$ ML deposit produces a ($\sqrt{3}$ x $\sqrt{3}$) R30° reconstruction, whereas a 1 ML deposit produces the ($2\sqrt{3}$ x $2\sqrt{3}$) R30° reconstruction. A schematic phase diagram

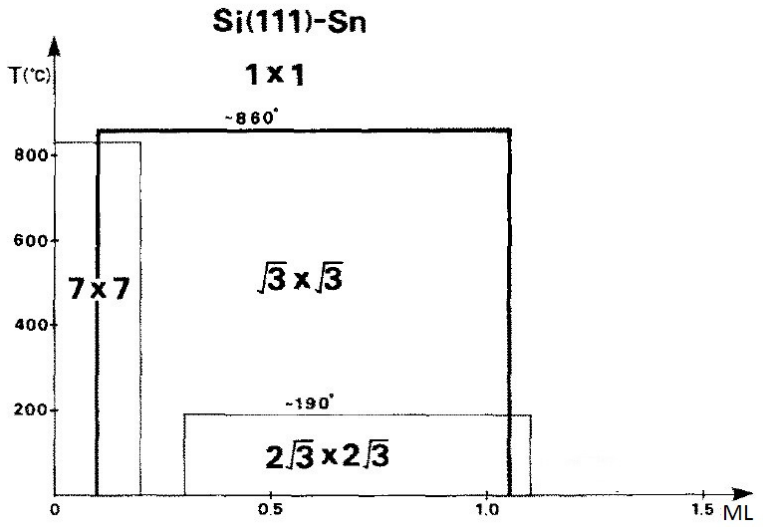

Figure 4.1: Phase diagram of (sub)monolayer phases of Sn on Si(111) (Ichikawa, 1984)

is shown in Figure 4.1. The ($\sqrt{3}$ x $\sqrt{3}$) R30° structure is well known. Here, the Sn adatoms occupy the T_4 adatom sites above the Si atoms in the second layer, as shown in Figure 4.2, thus forming a ($\sqrt{3}$ x $\sqrt{3}$) R30° arrangement of Sn atoms. The structure of the ($2\sqrt{3}$ x $2\sqrt{3}$) R30° phase is still under dispute. Our effort focuses on the LEED I(V) structure determination of the ($2\sqrt{3}$ x $2\sqrt{3}$) R30° reconstruction with and without the presence of boron dopants underneath (see also Chapter 1).

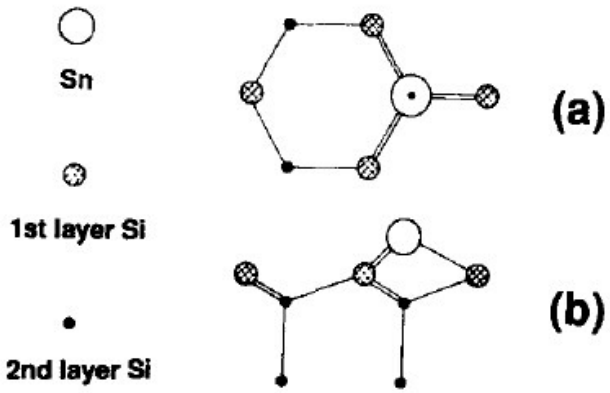

Figure 4.2: Top view and cross-sectional view of Sn on Si (111) ($\sqrt{3}$ x $\sqrt{3}$) R30° (Lin et al., 1996)

4.1.2 Proposed structure models for the Si(111) ($2\sqrt{3}$ x $2\sqrt{3}$) R30° reconstruction

Current structure models have slightly different compositions but share a common ingredient, that is, the ($2\sqrt{3}$ x $2\sqrt{3}$) R30° reconstruction consists of two atomic Sn layers on a bulk terminated Si(111) substrate. There are 4 Sn atoms per unit cell in the topmost layer which are clearly visible in the STM images. Disagreement exists about the number of Sn atoms below the top layer. In the model of Tornevik *et al.* in Figure 4.3 (Tornevik et al., 1991), there are ten atoms in the first layer and four atoms in the topmost layer. Hence the Sn coverage is 14/12 = 1.17 ML. (Note that a Si(111)1x1 unit cell contains one surface atom; hence a ($2\sqrt{3}$ x $2\sqrt{3}$) R30° supercell contains 12 atoms). The first layer contains a Sn-Sn dimer. Counting the bonds, it is clear that the dimer atoms have only one backbond, suggesting that they are absorbed right on top of a Si atom. The other six Sn atoms in the first layer surrounding the

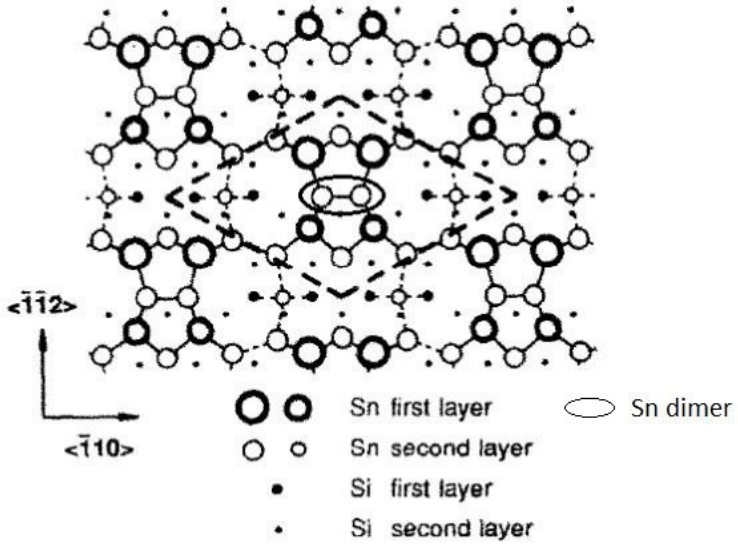

Figure 4.3: Top view of the Tornevik model for the ($2\sqrt{3}$ x $2\sqrt{3}$) R30° reconstruction of Sn on Si (111). Lines between atoms symbolize bonds. Further possible bonds, besides the dimer and adatom bonds, are marked with dashed lines. The thick dashed lines in the middle of the figure mark the ($2\sqrt{3}$ x $2\sqrt{3}$) unit cell. (Tornevik et al., 1994)

.

central Sn-Sn dimer are displaced outwards so as to form a local structure with in-plane distances close to those of α-Sn . Each of these eight Sn atoms (the previous six plus the two dimer atoms) eliminate one Si dangling bond. The two other Sn atoms left and right of the central dimer are postulated to be placed in bridge sites so as to eliminate the remaining Si dangling bonds. Finally, four Sn adatoms are placed in the top layer, which supposedly are the ones observed in the STM images. In all, the structure can be seen as consisting of locally complete α-Sn (111) double-layer subunits, where the deviations from the ideal bond angles are rather small (Tornevik et al., 1991). The total number of half-filled dangling bonds per ($2\sqrt{3}$ x $2\sqrt{3}$) R30° unit cell amounts to six, meaning that the total number of half-filled dangling bonds is reduced by a factor of two compared to that of the bulk terminated Si(111)1x1 surface. As such, the structure is expected to be reasonably stable.

In another model proposed by Eriksson at *et al.*, the first Sn layer contains only eight Sn atoms whereas the second layer again contains four Sn atoms. This structure is shown in Figure 4.4 (Eriksson et al., 2010). In this model, the total Sn coverage is (8+4)/12 = 1.0 ML.This structure seems more consistent with detailed STM images

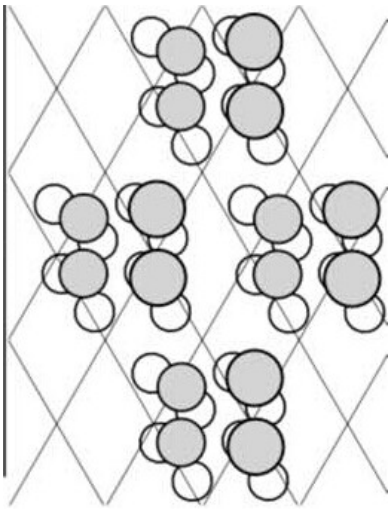

Figure 4.4: Schematic illustration of Eriksson's model of Si(111) ($2\sqrt{3}$ x $2\sqrt{3}$) R30°-Sn. The underlayer and top layer are represented by white and gray circles. The grid vertices correspond to the positions of the Si atoms (Eriksson et al., 2010)

of the first layer atoms, and with angle-resolved photoemission data, but it appears less intuitive.

The third model was proposed by Toshihiro Ichikawa (Ichikawa and Cho, 2003). This model contains 13 Sn atoms per ($2\sqrt{3}$ x $2\sqrt{3}$) R30° unit cell. The structure was optimized using an *ab initio* structure relaxation calculation. It explains the measured x-ray diffraction intensities, the 2D Pattern map, and scanning tunneling images (Ichikawa and Cho, 2003). As we can see in Figure 4.5, the top layer is identical to the other models showing two adatom pairs (1,1') and (2,2') that are observed in the STM images. There is another pair of Sn atoms located at the (4,4') position which is located 0.17$\mathring{A}$ below pair (1,1'). The other three adatom pairs and the lone Sn adatom at position (7) are located at deeper locations (Sugimoto et al., 2006). All in all, the total atom count is 9+4=13, resulting in a coverage of 13/12=1.08 ML.

None of these models turned out to be stable, according to the *ab initio* density functional theory calculations by our collaborator Dr. Paul Kent at ORNL. Further experimental input is thus required.

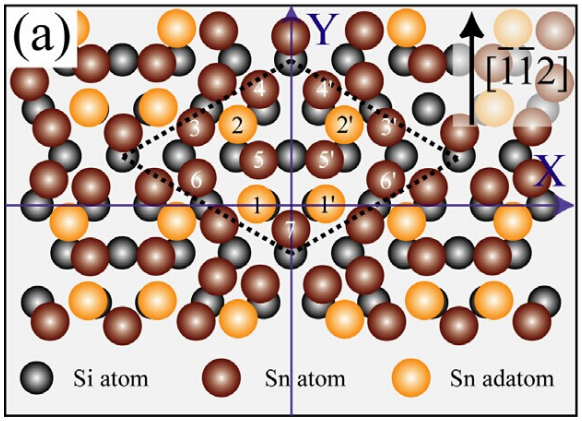

Figure 4.5: Ichikawa's model of Si(111) ($2\sqrt{3}$ x $2\sqrt{3}$) R30°-Sn space (Sugimoto et al., 2006)

4.1.3 Experimental results

Experiments were performed in an Omicron ultra-high vacuum chamber with a base pressure around 5x10^{-11} Torr. We used a n-type silicon wafer, which was cleaned by acetone and then ethanol prior to insertion into the UHV system. After we load the silicon into the chamber, we run a direct current of several amperes through the sample. This way, the sample can easily be heated to 1200 °C while minimizing degassing from the sample holder and manipulator head. We first degas the sample at 600 °C for 6 to 8 hours. Then we flash the sample to 1200 °C 20 times to remove the oxide layer and carbide particles. This short flash is followed by a five minute anneal at 950 °C so as to produce a clean well-ordered Si (111)7x7 surface. The LEED pattern, shown in Figure 4.6a, was recorded at room temperature and shows a sharp 7x7 diffraction pattern. 99.99 percent pure Sn was evaporated from a effusion cell and deposited onto a clean Si (111)7x7 substrate, kept at 450 °C. We first determined the deposition time needed to prepare a well-ordered ($\sqrt{3}$ x $\sqrt{3}$) R30° surface. The coverage of this reconstruction is known to be $\frac{1}{3}$ ML and thus we can we use this reconstruction to calibrate the deposition rate of Sn. If the surface is fully covered with the ($\sqrt{3}$ x $\sqrt{3}$) R30° phase and no Sn is lost due to reevaporation into the vcauum, we know exactly how much time it takes to deposit $\frac{1}{3}$ ML. The quality of

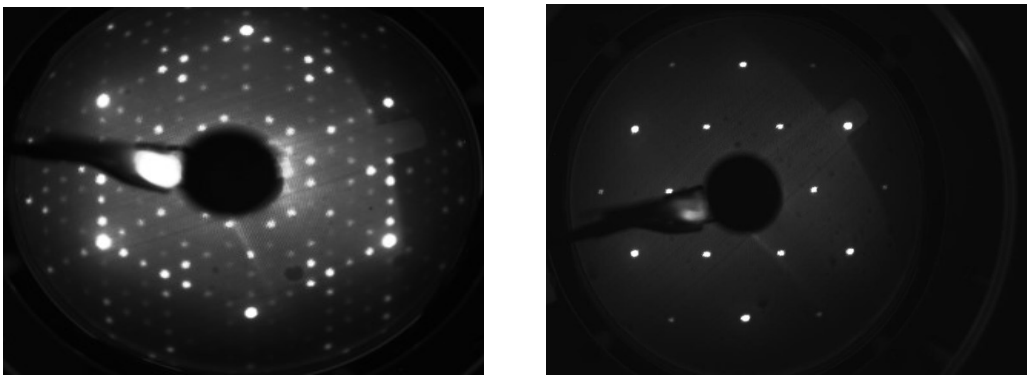

(a) 7 x 7 **(b)** $\sqrt{3}$ x $\sqrt{3}$ R30°

Figure 4.6: LEED pattern of the Si(111)7 x 7 and Si(111) ($\sqrt{3}$ x $\sqrt{3}$) R30°-Sn superstructure before and after deposition of $\frac{1}{3}$ ML of tin

this surface was checked with both LEED and STM. Figure 4.6b shows a sharp ($\sqrt{3}$ x $\sqrt{3}$) R30° LEED pattern while STM images reveal large (> 300 nm) terraces that are fully covered with the ($\sqrt{3}$ x $\sqrt{3}$) structure (Figure 4.7c). The coverage of this surface was also determined from the intensity ratio of the Sn-3$d_{\frac{5}{2}}$ and Si-2p core levels in XPS; see Figure 4.8. For a $\frac{1}{3}$ ML Sn deposit on Si (111) surface, this ratio should be 0.34 according to a simple layer-by-layer attentuation model of the XPS intensities. The measured ratio was 0.34, *i.e.*, very close.

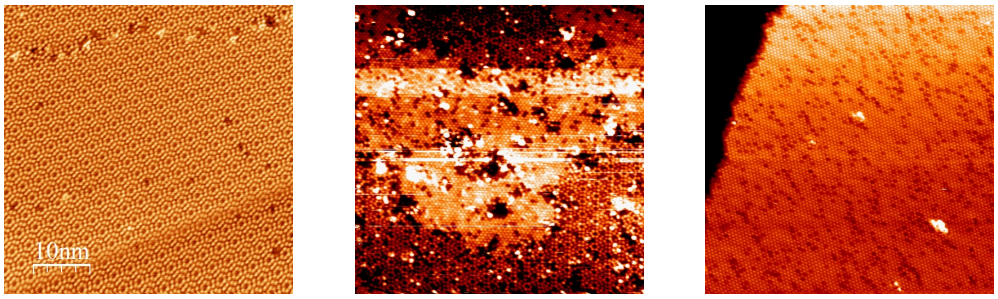

(a) clean silicon

(b) deposit less than $\frac{1}{3}$ ML tin

(c) deposit less $\frac{1}{3}$ ML tin

Figure 4.7: STM image of the Si(111)7 x 7 and Si(111) ($\sqrt{3}$ x $\sqrt{3}$) R30° superstructure before and after deposition of $\frac{1}{3}$ ML of tin.

Knowing the deposition rate with good accuracy, we set out to prepare the Si(111) ($2\sqrt{3}$ x $2\sqrt{3}$) R30°-Sn surface. There are two methods for growing this surafce. The first way is to deposit Sn on the surface at room temperature and to subsequently anneal the film at about 600 °C for two minutes. The second way is to grow Sn on a hot substrate at about 400 °C to 450 °C. Based on our LEED and STM investigations, we find that the latter method produces better ordered surfaces (Tornevik et al., 1991), which is very important for the LEED I(V) investigations. Because Sn partially re-evaporates at these annealing temperatures, we overexposed the Si(111) surface to the incoming Sn flux by about a factor of three. Hence, the precise coverage of the ($2\sqrt{3}$ x $2\sqrt{3}$) R30°-Sn surface cannot be inferred from the deposition time, but a similar XPS intensty analysis indidated that the coverage is close to 1.0 ML. After deposition, we annealed the sample at 450 °C for about five minutes and then slowly cooled the

sample down to room temperature. LEED and STM were used to check the quality of the surface. The LEED pattern showed a sharp ($2\sqrt{3}$ x $2\sqrt{3}$) R30° superstructure, as shown in Figure 4.9a. STM images revealed large (1000 nm^2) ($2\sqrt{3}$ x $2\sqrt{3}$) terraces, as shown in Figure 4.9b. The quality of this surface was deemed sufficient for a detailed LEED I(V) study, which will be discussed in Section 4.3.2

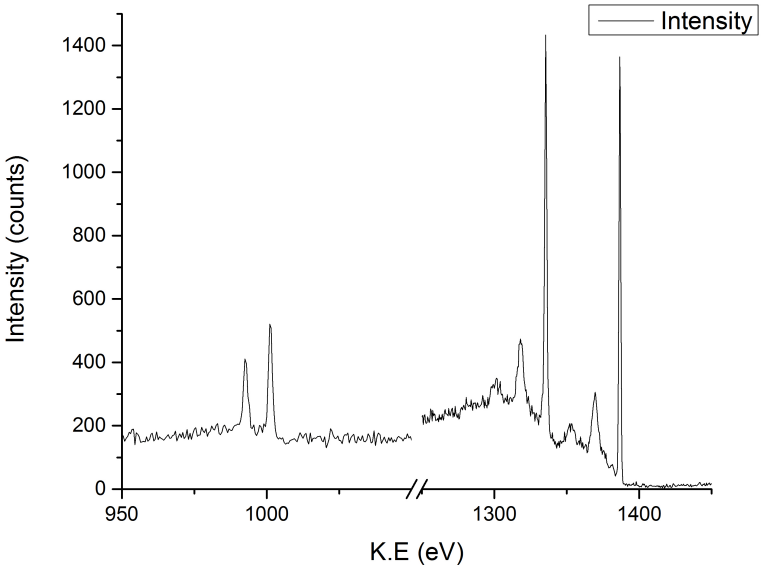

Figure 4.8: The XPS spectra of 1/3 ML Sn deposition on n-type Si, the ratio of the peak areas of the Sn-3$d_{\frac{5}{2}}$ and Si-2p core level spectra is close to 0.34

4.2 Preparation of the boron doped Si(111) substrate

4.2.1 Structure of the Si(111) ($\sqrt{3}$ x $\sqrt{3}$) R30°-B surface

As we discussed in Chapter 1, the Si(111) ($\sqrt{3}$ x $\sqrt{3}$) R30°-B surface has a unique configuration where the boron atoms occupy the S_5 subsurface site instead of usual T_4 adatom site, as shown in Figure 4.10 (Cao et al., 1993).

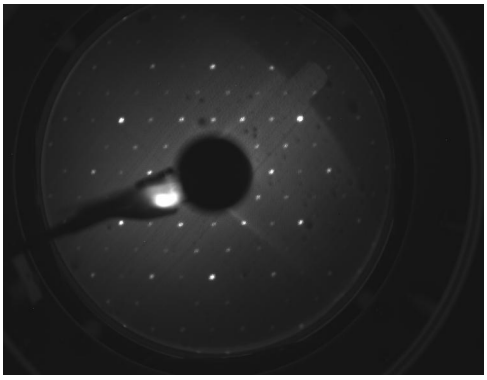

(a) LEED pattern $2\sqrt{3}$ x $2\sqrt{3}$ R30° superstructure

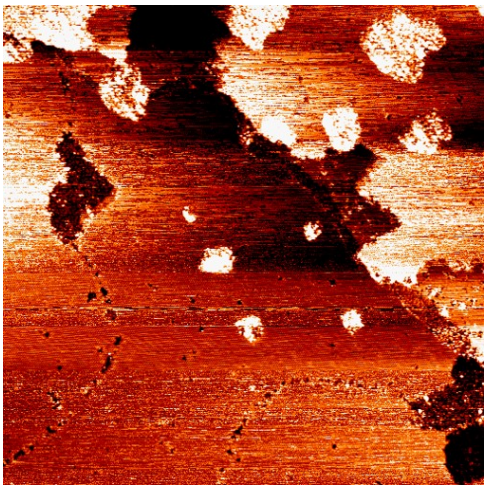

(b) STM image of $2\sqrt{3}$ x $2\sqrt{3}$ with $1000nm^2$ terrace

Figure 4.9: LEED pattern and STM image of ($2\sqrt{3}$ x $2\sqrt{3}$) R30° surface by depositing 1 ML Sn atoms on n-type Si(111).

According to DFT calculations, the S_5 site is favored over the T_4 site by 0.93 eV per ($\sqrt{3}$ x $\sqrt{3}$) R30° unit cell, or 0.31eV per 1x1 unit cell(Bedrossian et al., 1989). This is a very large number which has been attributed to the smaller covalent radius of the boron atom (as compared to the covalent radius of Si). The other Group (III) elements have a covalent radius larger than silicon and thus prefer to adsorb on top.

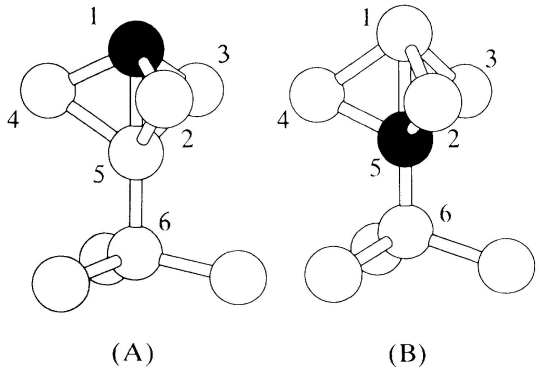

Figure 4.10: The black solid balls represents the Boron atoms while the white solid balls represents the Silicon atoms. Panel a is the structure of the T_4 adatom, and panel b is the structure of S_5 adatom. In boron doped silicon, the boron atom is located at the S_5 positon as shown in panel b (Bedrossian et al., 1989)

The B-Si bond is about 12 percent shorter than the Si-Si bond and the bond-angle stress is reduced by relaxing atoms 2, 3 and 4 inward, which decreases their separation by 10 percent relative to the bulk atomic spacing (Bedrossian et al., 1989).

4.2.2 Preparation of the boron doped Si(111) ($\sqrt{3}$ x $\sqrt{3}$) R30° surface

There are several ways to create a boron doped silicon ($\sqrt{3}$ x $\sqrt{3}$) R30° surface, for instance by direct deposition of boron onto Si(111) (Cao et al., 1993). In our experiment, we created this reconstruction by annealing a heavily boron doped silicon(111) wafer (about 4 mOhm·cm) to 950 °C in UHV for a couple of hours, (Bensalah et al., 1989) established a correlation between the annealing temperature and boron concentration in the surface layer, as shown in Table 4.1.

The preparation of this surface was performed in an Omicron ultra-high vacuum chamber with a base pressure around 5 x 10^{-11} Torr. Before loading the sample into the vacuum chamber, we dipped the sample in acetone and ethanol for about 10 and

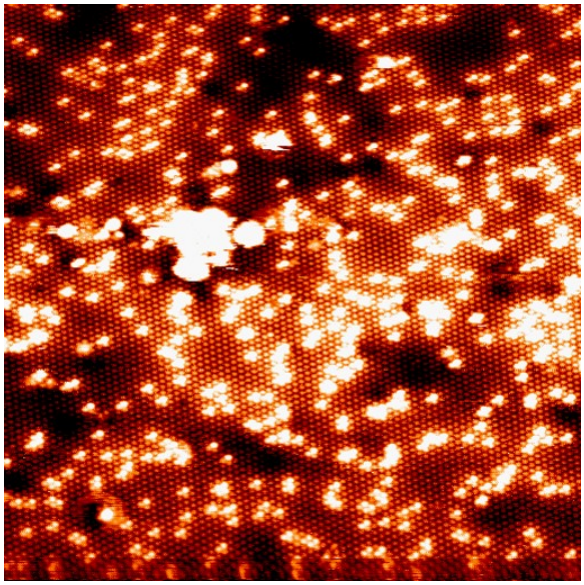

Figure 4.11: The STM image of a boron doped Si(111) ($\sqrt{3}$ x $\sqrt{3}$) R30° surface. The tiny atoms in the image are Si atoms with boron atoms underneath. Bright spots are most likely clusters of excess Si on the surface

5 minutes, respectively. Next, the sample was heated by direct current heating to 550 °C and degassed for about 6 to 8 hours. After the degassing procedure, we flashed the sample to 1200 °C for about 10 to 15 times. Then we annealed our sample at 1150 °C for about 2 hours and then slowly decreased the temperature to 950 °C at a rate of about 1 °C per min. We stayed at that temperature for 1 hour and then decreased the temperature to room temperature relatively slowly (about 5 °C per min above 400 °C). During the entire procedure, we kept the pressure in chamber in the 10^{-10} Torr range by cooling the manipulator with liquid nitrogen. The temperature of the surface was monitored by a parameter, which works accurately above 400 °C. After the procedure, we used LEED and STM to check the quality of the surface. A near perfect surface may require one or more repetitions of this annealing procedure.

Table 4.1: Boron concentration after different temperature anneals (Bensalah et al., 1989)

Thermal treatment	LEED pattern structure	Si(au)	B/B sat
640°C, 10 mins	7 x 7	1	0
920°C, 10 mins	trace 7 x 7	0.95	0.16
1080°C 11 mins	1 x 1	0.90	0.45
1150°C 15 mins	$\sqrt{3}$ x $\sqrt{3}$ R30°	0.95	1
1150°C 60 mins	$\sqrt{3}$ x $\sqrt{3}$ R30°	0.95	1

4.3 Acquisition of LEED I(V) data from the Si(111) ($2\sqrt{3}$ x $2\sqrt{3}$) R30°-Sn surface with and without boron underlayer

4.3.1 Experiment

After obtaining a well prepared Si(111) ($\sqrt{3}$ x $\sqrt{3}$) R30° surface with a boron underlayer, we deposited 1 ML Sn atoms on this surface to obtain the ($2\sqrt{3}$ x $2\sqrt{3}$) R30° surface. Again, we used LEED and STM to check the quality the surface. A

sharp ($2\sqrt{3}$ x $2\sqrt{3}$) R30° LEED pattern is shown in Figure 4.12. STM images reveal the presence of over 1000 nm^2 terraces with the ($2\sqrt{3}$ x $2\sqrt{3}$) structure, as shown in Figure 4.13, thus indicating good surface quality. XPS analysis indicates that the Sn coverage on the doped and undoped surfaces are identical within the margin of error, see (Figure 4.14). Finally, we acquired a LEED I(V) data set with beam voltages ranging from from 50 eV to 500 eV with 2 eV increments. During the LEED IV measurements, we cooled down the sample to 90 K, using liquid nitrogen. This was done to reduce the diffuse background on the screen so that we could trace the LEED spots to higher energy. The larger the data set, the more reliable the LEED I(V) structure determination.

To record the intensity of the spots as a function of beam voltage, we use a CCD camera and imported the camera images with a program called 'easy leed', written by Python. In this program, we can select different spots and the program will automatically track the spots with changing beam voltage and plot their intensities. We selected several groups of symmetry equivalent spots from the ($2\sqrt{3}$ x $2\sqrt{3}$ R30°) surface both on n-type and p-type silicon, then averaged the symmetry equivalent beams, and subsequently compared their I(V) spectra.

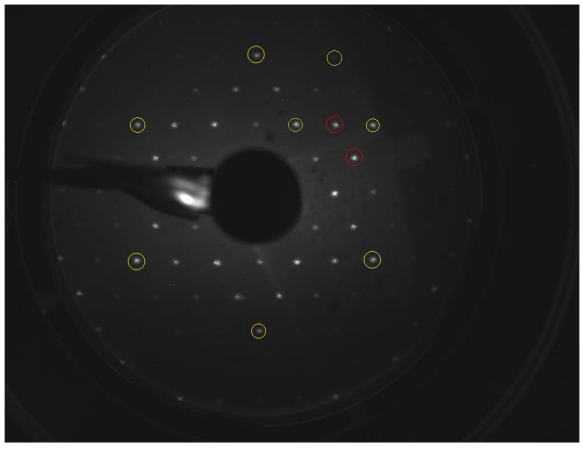

Figure 4.12: LEED pattern of the Si(111) ($2\sqrt{3}$ x $2\sqrt{3}$) R30°-Sn superstructure with a beam energy of 50 eV. The spots inside the yellow circle are the (1,0) and (0,1) integer order beams; The spots inside the green circle are the $\sqrt{3}$ spots ($\frac{1}{3}$, $\frac{1}{3}$),($\frac{2}{3}$, $\frac{2}{3}$); The spots inside the red red circles are the $2\sqrt{3}$ reflections ($\frac{1}{6}$, $\frac{2}{3}$),($\frac{2}{3}$, $\frac{1}{6}$)

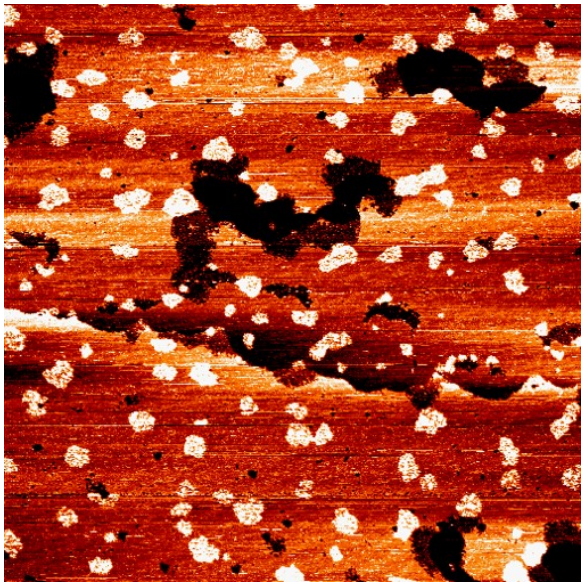

Figure 4.13: The STM image of the Si(111) ($2\sqrt{3}$ x $2\sqrt{3}$) R30°-Sn reconstruction, showing 1000 nm^2 terraces

4.3.2 LEED I(V) result and discussion

The original LEED I(V) spectra are similar to those in Figure 2.5. Before we perform some quantitative analysis, we need to smooth the I(V) spectra. Figure 4.15 compares the I(V) spectra of identical beams, recorded from the n-type and p-type samples.

Notice that there is a big difference in the absolute intensities of peaks when comparing the n- and p-type samples. This might be caused by differences in screen voltage, CCD aperture or surface quality. However, notice that the peak positions are basically identical, meaning that the atomic structures are almost identical. For better comparison, we normalized the intensity scale to the maximum peak intensity.

Figure 4.16 shows the I(V) spectra after normalization. From the Figure, we can see the (1, 0) beams of the n- and p-type sample are effectively identical. The (0,1) beams are almost exactly the same except in the range between 250 eV to 300 eV.

We also monitored the ($\sqrt{3}$ x $\sqrt{3}$) spots. Here, we selected the ($\frac{1}{3}$, $\frac{1}{3}$) and ($\frac{2}{3}$, $\frac{2}{3}$) spots, and we noticed an interesting shift between those two curves in Figure 4.17. Specifically, there is a small difference in the peak location near 250 eV. Dynamical

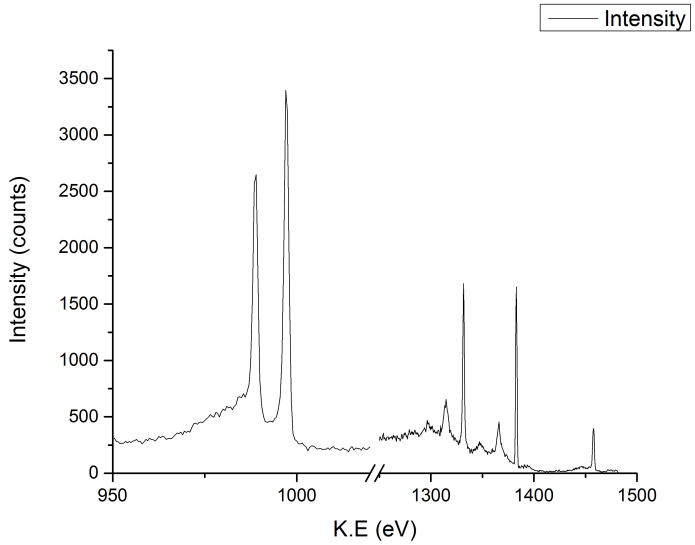

(a) The XPS spectra of 1 ML Sn on n-type Si

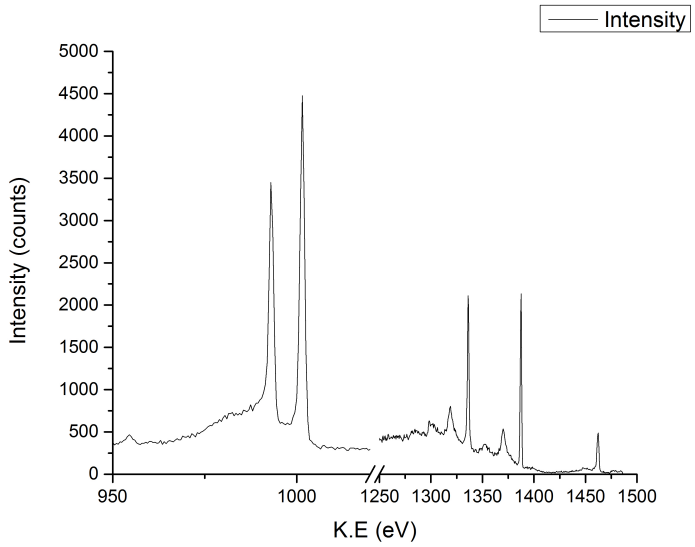

(b) The XPS spectra of 1 ML Sn on p-type Si

Figure 4.14: XPS spectra of the Si(111) ($2\sqrt{3}$ x $2\sqrt{3}$) R30°-Sn surface on n-type Si and p-type Si. The intensity ratios of the Sn-3$d_{\frac{5}{2}}$ and Si-2p core level spectra are almost identical

LEED I(V) simulations show that the precise location of the $\frac{1}{3}$ order beams depends on the presence or absence of boron at the S_5 lattice location.

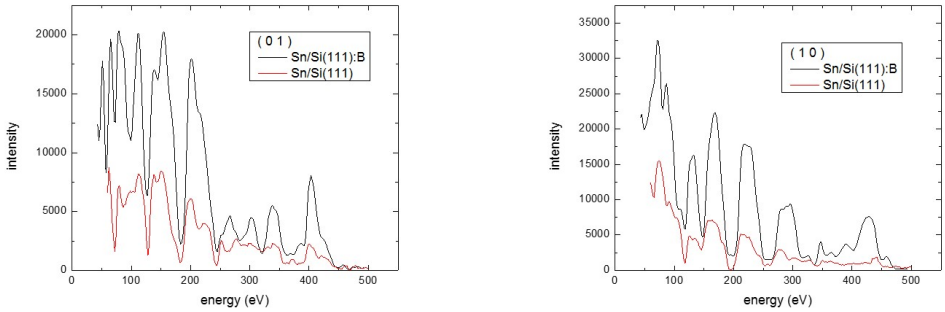

(a) The curve of (0,1) spot **(b)** The curve of (1,0) spot

Figure 4.15: LEED I(V) curve of the (1,0),(0,1) spots of the Si(111) ($2\sqrt{3}$ x $2\sqrt{3}$) R30°-Sn reconstruction on n- and p-type Si(111), before normalization (R. Diehl, unpublished result)

Finally, we measured the ($2\sqrt{3}$ x $2\sqrt{3}$) spots, and selected the ($\frac{1}{6}$, $\frac{2}{3}$) and ($\frac{2}{3}$, $\frac{1}{6}$) in Figure 4.18 for comparison. Again, the beams are almost identical, meaning that the structure of the Sn layers on n- and p-type Si(111) is very similar.

In conclusion, our LEED IV data show that the (1,0) and (0,1) integer order spots and the ($2\sqrt{3}$ x $2\sqrt{3}$) spots ($\frac{1}{6}$, $\frac{2}{3}$),($\frac{2}{3}$, $\frac{1}{6}$ are almost identical for the Sn bilayers grown on n-type silicon and boron doped silicon. For the ($\sqrt{3}$ x $\sqrt{3}$) spots, we observe a small

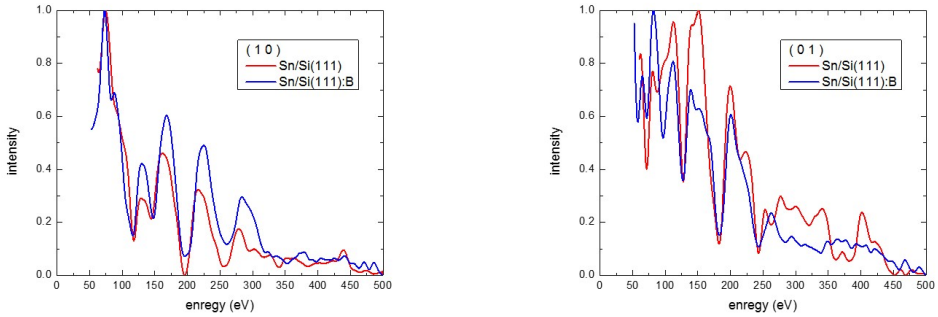

(a) The curve of (1,0) spot **(b)** The curve of (0,1) spot

Figure 4.16: LEED I(V) curve of the (1,0),(0,1) spots of the Si(111) ($2\sqrt{3}$ x $2\sqrt{3}$) R30°-Sn reconstruction on n- and p-type Si(111), after normalization (R. Diehl, unpublished results)

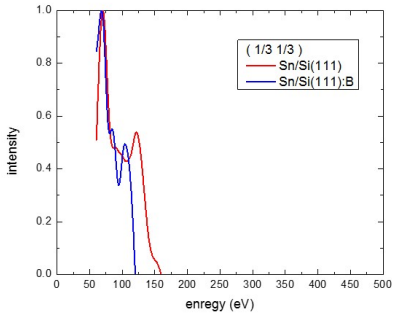

(a) The curve of $(\frac{1}{3}, \frac{1}{3})$ spot

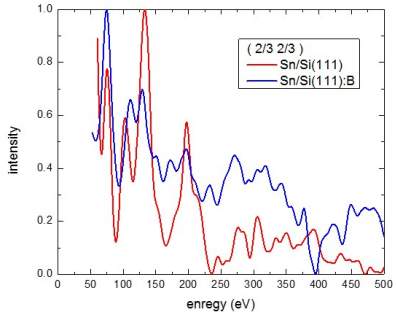

(b) The curve of $(\frac{2}{3}, \frac{2}{3})$ spot

Figure 4.17: LEED I(V) spectra of the Si(111) $(2\sqrt{3}$ x $2\sqrt{3})$ R30°-Sn reconstruction on n- and p-type Si(111), after normalization (R. Diehl, unpublished results)

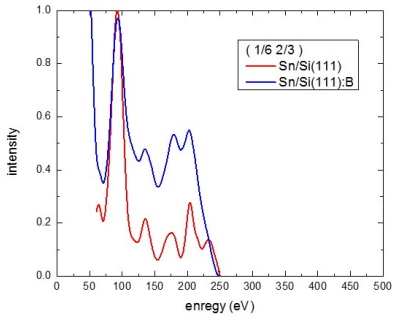

(a) The curve of $(\frac{1}{6}, \frac{2}{3})$ spot

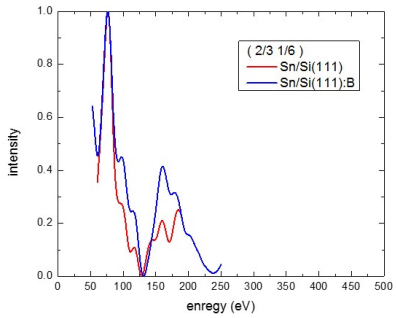

(b) The curve of $(\frac{2}{3}, \frac{1}{6})$ spot

Figure 4.18: LEED I(V) spectra of the Si(111) $(2\sqrt{3}$ x $2\sqrt{3})$ R30°-Sn reconstruction on n- and p-type Si(111), after normalization (R. Diehl, unpublished results)

energy shift between the I(V) spectra of the two surfaces. This is likely due to the presence of boron at the S_5 lattice location beneath the Sn layer in the case of boron doped Si(111). We conclude that the atomic structures of the Si(111) $(2\sqrt{3}$ x $2\sqrt{3})$ R30°-Sn reconstruction on n-type and p-type Si are basically identical. Nonetheless, the exact structure is still unknown.

From the fitting of our data to a dynamical LEED I(V) structure code, which is currently being conducted by Prof. Renee Diehl's group at Penn State University, it appears that the model of Ichikawa produces the lowest Pendry R-factor. Right now,

it is 0.44 but we would like it to be much smaller, maybe close to 0.3. A possible next step is to enter the atomic coordinates from the LEED I(V) study into a first principles density functional theory code to relax the structure to a new total-energy minimum. The new theoretical coordinates can then be used in the LEED I(V) code and fitted against our experimental results. This process should be iterated until acceptable agreement is found.

Bibliography

Avila, J., Mascaraque, A., Michel, E. G., Asensio, M. C., LeLay, G., Ortega, J., and Flores, F. (1999). Dynamical fluctuations as the origin of a surface phase transition in Sn/Ge (111). *Physical Review Letters*, 82.2:442. 5

Bedrossian, P., Meade, R. D., Mortensen, K., Chen, D. M., Golovchenko, J. A., and Vanderbilt, D. (1989). Surface doping and stabilization of Si (111) with boron. *Physical Review Letters*, 63.12:1257. xiii, 42, 43

Bensalah, S., Lacharme, J. P., and Sebenne, C. A. (1989). $\sqrt{3}$ x $\sqrt{3}$ reconstruction along the (111) face of highly boron-doped Si upon vacuum annealing. *Surface Science*, 211:586–592. x, 43, 44

Bogart, T. F., Beasley, J. S., and Rico, G. (2004). *Electronic devices and circuits.* Pearson/Prentice Hall. xi, 2

Boyle, W. S. and Smith, G. E. (1970). Charge coupled semiconductor devices. *Bell System Technical Journal*, 49.4:587–593. 29

Cao, R., Yang, X., and Pianetta, P. (1993). Characterization of the B doped Si surface electronic structure. *Journal of Vacuum Science and Technology*, A 11.4:1817–1822. 4, 41, 43

Chen, C. J. (1993). *Introduction to scanning tunneling microscopy.* Oxford UniverSity Press. 30

Eriksson, P. E. J., Osiecki, J. R., Sakamoto, K., and Uhrberg, R. I. G. (2010). Atomic and electronic structures of the ordered $2\sqrt{3}$ x $2\sqrt{3}$ and molten 1 x 1 phase on the Si (111):Sn surface. *Physical Review B*, 81.23:5410. xiii, 4, 37

Flores, F., Ortega, J., and Perez, R. (1999). Many-body effects and the metal insulator transition at semiconductor surfaces and interfaces. *Surface Review and Letters*, 6.03n04:411–433. 3

Goodman, C. H. L. (1982). *Solid State and Electronic Devices.* IEE Proc. 2

Ichikawa, T. (1984). Structural study of ultrathin Sn layers deposited onto Ge (111) and Si (111) surfaces by RHEED. *Surface Science*, 140.1:37–63. xii, 35

Ichikawa, T. and Cho, K. (2003). Structural study of Si (111) ($2\sqrt{3}$ x $2\sqrt{3}$) R30°Sn surfaces. *Japanese Journal of Applied Physics*, 42.8R:5239. vi, 4, 38

Lee, P. A., Nagaosa, N., and Wen, X. G. (2006). Doping a Mott insulator: Physics of high-temperature superconductivity. *Reviews of Modern Physics*, 78.1:17. 3

Lin, X. F., Chizhov, I., Mai, H. A., and Willis, R. F. (1996). Scanning tunneling spectroscopy examination of surface electronic structures of Si (111) ($2\sqrt{3}$ x $2\sqrt{3}$) R30° -Sn surface. *Applied Surface Science*, 104:223–227. xii, 35

Luth, H. (2010). *Solid Surfaces, Interfaces and Thin Films (Fifth Edition).* Springer-Verlag Berlin Heidelberg. xi, xii, 8, 9, 12, 13, 14, 23, 24, 26, 30

Lyo, I., Kaxiras, E., and Avouris., P. (1989). Adsorption of boron on Si (111): Its effect on surface electronic states and reconstruction. *Physical Review Letters*, 63.12:1261. 3

Morris, A. L., MacArthur, M. W., Hutchinson, E. G., and Thornton, J. M. (1992). Stereochemical quality of protein structure coordinates. *Proteins: Structure, Function, and Bioinformatics*, 937:44. 19

Ortega, J., Perez, R., and Flores, F. (2002). Dynamical fluctuations and the $\sqrt{3}$ x $\sqrt{3}$ to 3 x 3 transition in α-Sn/Ge (111) and Sn/Si (111). *Journal of Physics: Condensed Matter*, 14.24:5979. 5

Oura, K., Zotov, A. V., Lifshits, V. G., Saranin, A. A., and Katayama, M. (2003). *Surface science: an introduction*. Berlin, Heidelberg: Springer. xii, 30, 31, 32

Pendry, J. B. (1974). *Low energy electron diffraction.* SERC Daresbury Laboratory MUFPOT program. 28

Pendry, J. B. (1980). Reliability factors for LEED calculations. *Solid State Physics*, 12.4:346–364. 19, 20

Redhead, P. A., Hobson, J. P., and Kornelsen, E. V. (1993). *Physical basis of ultrahigh vacuum.* AIP, Newyork. 24

Schubert, E. F. (1993). *Doping in III-V semiconductors Vol. 27.* Cambridge University Press. 1

Seah, M. P. and Dench, W. A. (1979). Quantitative electron spectroscopy of surfaces: a standard data base for electron inelastic mean free paths in solids. *Surface and Interface Analysis*. xii, 18

Sugimoto, Y., Abe, M., Hirayama, S., and Morita, S. (2006). Highly resolved non-contact atomic force microscopy images of the Sn/Si (111)-($2\sqrt{3}$ x $2\sqrt{3}$) R30° surface. *Nanotechnology*, 17.16:4235. xiii, 38

Tornevik, C., Gothelid, M., Hammar, M., Karlsson, U., Nilsson, N., Flodstriim, S., Wigren, C., and Ostling, M. (1994). Adsorption of Sn on Si (111) 7x7 reconstruction in the monolayer regime. *Surface Science*, 314:179–187. xiii, 36

Tornevik, C., Hammar, M., Nilsson, N. G., and Flodstrom, S. A. (1991). Epitaxial growth of Sn on Si (111): A direct atomic-structure determination of the ($2\sqrt{3}$ x $2\sqrt{3}$) R30° reconstructed surface. *Physical Review B*, 44:23. 34, 36, 37, 40

Tosatti, E. and Anderson, P. W. (1974). Charge and spin denSity waves on semiconductor surfaces. *Japanese Journal of Applied Physics*, 13.S2:381. 3

Tosatti, E., Bertel, E., and Donath, M. (1995). *Electronic Surface and Interface States on Metallic Systems*. World Scientific, Singapore. 3

VanHove, M. A., Weinberg, W. H., and Chan, C. M. (1986). Low-energy electron diffraction. *Surface Science*, 6:155–177. xi, 8, 12, 15

Wood, E. A. (1964). Vocabulary of surface crystallography. *Journal of Applied Physics*, 35.4:1306–1312. 8

Vita

Weisong Tu was born in Jinan, Shandong province in China on July 9th, 1987. He attended to Shandong Normal University (SDNU) for undergraduate study in 2006. In 2008, he transferred to East Tennessee State University (ETSU) in Johnson City, TN. In 2010, he graduated from ETSU and earned a degree of Bachelor of Science in Physics. At the same time, he also received Bachelor degree in Applied Physics from SDNU. He was admitted by the graduate school in The University of Tennessee, Knoxville in the same year and started his masters project in 2011. His project is concentrated on structure analysis of Sn bilayer films on both p-type and n-type silicon. He expects to graduate with a Masters degree in Physics in July 2014.